
SEISMIC MONITORING OF CO₂ PLUME DYNAMICS USING ENSEMBLE KALMAN FILTERING

Grant Bruer

School of Computational Science and Engineering
Georgia Institute of Technology
Atlanta, GA 30332 USA

Abhinav Prakash Gahlot

School of Earth and Atmospheric Sciences
Georgia Institute of Technology
Atlanta, GA 30332 USA

Edmond Chow

School of Computational Science and Engineering
Georgia Institute of Technology
Atlanta, GA 30332 USA

Felix Herrmann

School of Computational Science and Engineering
Georgia Institute of Technology
Atlanta, GA 30332 USA

October 22, 2024

ABSTRACT

Monitoring carbon dioxide (CO₂) injected and stored in subsurface reservoirs is critical for avoiding failure scenarios and enables real-time optimization of CO₂ injection rates. Sequential Bayesian data assimilation (DA) is a statistical method for combining information over time from multiple sources to estimate a hidden state, such as the spread of the subsurface CO₂ plume. An example of scalable and efficient sequential Bayesian DA is the ensemble Kalman filter (EnKF). We improve upon existing DA literature in the seismic-CO₂ monitoring domain by applying this scalable DA algorithm to a high-dimensional CO₂ reservoir using two-phase flow dynamics and time-lapse full waveform seismic data with a realistic surface-seismic survey design. We show more accurate estimates of the CO₂ saturation field using the EnKF compared to using either the seismic data or the fluid physics alone. Furthermore, we test a range of values for the EnKF hyperparameters and give guidance on their selection for seismic CO₂ reservoir monitoring.

This work was supported by the National Science Foundation under Grant 2203821.

1 Introduction

Carbon capture and storage is a recently sought-after technology involving capturing carbon dioxide (CO₂) for long-term storage. Geologic storage sites such as saline aquifers and depleted oil fields can store large amounts of CO₂ due to their size and the naturally high pressure deep underground [1]–[3]. Monitoring the state of such CO₂ reservoirs is critical to avoid failure scenarios, such as leaks or man-made seismic activity (earthquakes) [4], [5]. Monitoring also enables real-time optimization of reservoir performance using computer simulations. However, due to the limited accessibility of underground reservoirs, traditional measurements of the reservoir state are confined to the surface and a relatively small number of boreholes compared to the size of the reservoir. This limits the predictive power of simulations that are based on traditional measurements. Since injected CO₂ replaces brine in saline aquifers, it affects the wave propagation in the rock, and the data from seismic waves reveal information at otherwise inaccessible points. Thus, seismic measurements provide a non-intrusive method for determining the spread of the CO₂ in saline aquifers, providing higher resolution estimates than other non-intrusive methods such as measurements of the electromagnetic or gravitational field [6]–[10].

This paper combines fluid-flow simulations with time-lapse full waveform seismic data to predict CO₂ saturations in underground reservoirs as CO₂ is injected. While most existing approaches use time-lapse seismic data by itself, the combination of physical simulation and full waveform seismic data has recently begun to be studied [11], [12]. Challenges that hinder progress in this area include the cost of the high-resolution physical simulations and the cost

of storing the covariance matrix necessary for properly combining information from the simulation and from system measurements. These problems have been tackled in other domains, such as weather forecasting, using algorithms such as ensemble Kalman filters, particle filters, and variational optimization. These methods are all forms of Bayesian data assimilation.

Bayesian sequential data assimilation aims to estimate a state vector over time with quantified uncertainty given a sequence of noisy time-lapse measurements. For our purposes, the state is the CO₂ saturation throughout the reservoir, and the measurements come from seismic waveform data. The state follows known two-phase flow dynamics with uncertainty coming from the unknown subsurface permeability field, which describes the rate at which the CO₂ and brine flow through the porous rock. To appropriately combine noisy time-lapse measurements with uncertain simulation predictions, we apply Bayesian sequential data assimilation. Specifically, we demonstrate the computational efficiency and the predictive efficacy of the ensemble Kalman filter (EnKF) technique on CO₂ reservoirs with multiple time-lapse surveyed seismic data.

The main issue with data assimilation for CO₂ reservoirs is that the sheer size of the problem makes the simulation and the data assimilation computations expensive. CO₂ reservoirs are represented in simulation by discretizing the reservoir into a three-dimensional grid and associating at the very least one CO₂ saturation value and one pressure value at each point in the grid. The system is governed by nonlinear dynamics, and thus demands a relatively high-resolution grid in order to be acceptably accurate. For example, a “small” reservoir can have a volume of 10¹⁰ cubic meters (equivalent to a few dozen cubic kilometers) and be broken into cells on the order of 10² ~ 10³ cubic meters. The state vector (the CO₂ saturation) has 10⁷ degrees of freedom. Seismic measurements are collected by recording seismic waves with a resolution of about 10⁻³ seconds (equivalent to a few milliseconds) for a duration on the order of a second. A “small” seismic survey records these waves for 10–100 sources for each of 100–1000 receivers, making the total length of the observation vector approximately 10⁸. While this is not prohibitively large for a single vector (a few hundred megabytes), data assimilation requires storing data many times that size, which can quickly cause issues with computation. In our experiments, we model a two-dimensional (2D) reservoir with volume ~ 10⁸ cubic meters, so the state vector is of size ~ 10⁵, and the observation vector is of size ~ 10⁶. For classical data assimilation techniques that require storing the square of the data size, this 2D system requires almost one hundred gigabytes of computer memory, while the three-dimensional 10¹⁰ cubic meter system requires more than one terabyte of memory.

A classical data assimilation technique is the *Kalman filter* (KF), which computes the optimal state for a given set of measurements assuming linear transition and measurement functions with Gaussian noise. With N_x as the length of the system state vector and N_y as the length of the measurement vector, the standard KF computes the Gaussian distribution of the state vector x in $O(N_x^2 + N_y^3)$ time and $O(N_x^2 + N_y^2)$ storage, excluding the cost of the simulations. Other data assimilation research on CO₂ reservoirs has handled the challenge of large covariance matrix sizes from seismic waveform observations by using a hierarchical sparse matrix structure [11], [13] or using ensemble-based methods [14] with the neighborhood algorithm [15]. However, these past data assimilation approaches with full waveform measurements of CO₂ reservoirs have ignored the CO₂ dynamics.

CO₂ reservoirs, like many real-world systems, are governed by nonlinear dynamics, which breaks the Gaussianity assumption of the KF. The KF can be successfully applied to nonlinear systems (in which case it is called the *extended* KF) if the time between measurements is so small that the transition is approximately linear. But the high cost of seismic surveys leads to a long time between reservoir measurements, which breaks the linear approximation. Furthermore, seismic observation is a nonlinear operator, further breaking the assumptions of the KF.

Weather forecasting is the well-researched domain that routinely handles nonlinearity, noise, and large data sizes for data assimilation. Major weather forecasting centers rely on various data assimilation algorithms, including variational methods such as *four-dimensional variational assimilation* (4D-Var) and ensemble methods such as the *ensemble Kalman filter* (EnKF).

Variational methods, on the one hand, minimize the observation error regularized with the distance from the predicted state. These methods can have a high implementation cost because they require adjoint operators for computing gradients. Additionally, for large systems, storing the state covariance matrix becomes infeasible. Bannister [16], [17] describes how weather forecasting models reduce the matrix storage size by diagonalizing the covariance matrix using a physics-based transform. However, this transform becomes less accurate as model resolutions increase, and as a result, many weather systems have switched to an ensemble-based estimate of the covariance. Furthermore, the variational methods do not estimate the posterior uncertainty, so they must be combined with ensemble methods to obtain a covariance estimate.

Ensemble methods, on the other hand, are comparatively much easier to implement because they do not require adjoint operators. The basic EnKF updates a sample of system states forward in time and uses the sample covariance to update the samples based on observations. Although this algorithm is optimal only for linear models, it does not

rely on linearizing the transition or observation models and thus handles nonlinearities much better than the standard KF. Furthermore, using a low-rank form for the covariance simplifies the update cost to $O(N_x N_e)$ for an ensemble of size N_e . The EnKF has been shown to scale well with N_x both in accuracy and computational cost for many data assimilation problems [18]–[20]. Several variants of the EnKF exist, such as those described by Evensen [21], but we leave other variants to future work.

In seismic measurement domains, several variations on the KF of varying complexity have been used to address nonlinearity, noise, and large data, but none yet have addressed the combination of large CO₂ reservoirs with CO₂ dynamics and full waveform seismic measurements. Eikrem *et al.* [22] address the issue of observation nonlinearity by using the iterated extended KF to estimate wave velocities from the full waveform data. This method linearizes the model at multiple points, thereby better approximating the nonlinearity, but they note it requires an adjoint observation model and the matrix storage causes difficulty for scaling to large data. Li *et al.* [23] address the issue of scalability with a low-rank KF to estimate CO₂ reservoir state. They show its performance on seismic travel time measurements or 115 wells on a small 0.2 square kilometers domain, but this method has not been shown on high-dimensional seismic data. Alfonzo and Oliver [24] apply the ensemble transform KF to estimate porosity based on acoustic impedance inverted from seismic measurements, but this does not estimate the dynamic state of the reservoir. Grana *et al.* [12], Guzman *et al.* [25], and Ma *et al.* [26] apply the EnKF to estimate CO₂ reservoir state and geological parameters using CO₂ dynamics but not full waveform observations. A scalable application of the KF using full waveform data and CO₂ dynamics has yet to be achieved.

In the machine-learning (ML) domain, research that uses CO₂ dynamics has focused on building surrogate flow models for use in Bayesian inversion algorithms to estimate static properties, such as porosity and permeability or some other parameter for the surrogate model [27]–[34]. The surrogate models allow the use of inversion algorithms that are more expressive but more expensive than the KF, for instance, rejection sampling [27]; randomized maximum likelihood [28], [29]; ensemble smoothing with multiple data assimilation (ES-MDA) [29]–[31]; and variational methods [32]–[34]. While one reference uses full-waveform seismic data [32], most do not, instead relying on less informative data such as well data [28], [29], [34] or surface deformation data [27], [31], while those using seismic data approximate the seismic image directly [30], [33]. We are also investigating ML-based DA research using full-waveform seismic data and CO₂ fluid dynamics; see [35], [36] for preliminary results. While ML-based methods show promise, they have not reached the level of robustness, scalability, and interpretability that the EnKF has shown in the field of weather forecasting.

In this research, we show that the EnKF with full waveform data and CO₂ dynamics estimates the CO₂ reservoir state with higher accuracy than two non-data-assimilation baselines without needing a prohibitively large ensemble. This study contributes to the broader objective of incorporating full waveform data and known physics into the scalable and computationally efficient EnKF. The paper is structured as follows: Section 2 describes the mathematical background for filters, two-phase flow, and seismic measurements; Section 3 describes how we structure the two-phase flow and seismic operators in the EnKF; Section 4 describes our high-dimensional synthetic experiment; Section 5 describes the results of our tests with the EnKF; and Section 6 concludes.

2 Background

2.1 Filters

Data assimilation is the process of estimating a hidden system state using available observations as well as knowledge of the system’s dynamics. The simulated dynamics are represented with the Markovian transition function f , which updates the state x^n at time step n to the next time step. System measurement is represented with the observation function h . Both functions may depend on noise η sampled at each time step independent of x , which represents any stochasticity of the system or unknown system dynamics. The transition and observation operators may depend on time, but we will typically omit the time parameters as they are clear in context. We also leave off the noise parameter as necessary when indicating a non-noisy evaluation. Mathematically, the operators are written as

$$x^{n+1} = f(x^n, \eta_f; t_n, t_{n+1}) \text{ and} \quad (1)$$

$$y^{n+1} = h(x^{n+1}, \eta_h; t_{n+1}), \quad (2)$$

with η_f and η_h being noise samples for f and h .

Using a sequence of observation data vectors $\{y^1, y^2, \dots, y^n\}$, data assimilation algorithms estimate the hidden states $\{x^1, x^2, \dots, x^n\}$. Typically, we are unable to observe the full hidden state, making this an ill-posed inverse problem

Algorithm 1: Generic data assimilation loop

Input: prior, data y^n at time t_n

```

1 posterior  $\leftarrow$  prior
2  $t_{n-1} \leftarrow 0$ 
3 for ( $y^n, t_n$ ) in observations do
4     // Equation (6)
4     prior  $\leftarrow$  Predict(posterior,  $t_{n-1}, t_n$ )
4     // Equation (7)
5     posterior  $\leftarrow$  Update(prior,  $y^n$ )
6      $t_{n-1} \leftarrow t_n$ 

```

requiring regularization. Regularization can be expressed as a prior distribution in Bayes' formula, which states

$$p(x|y) = \frac{p(y|x)p(x)}{p(y)}. \quad (3)$$

The prior $p(x)$ can be chosen based on physics or smoothness knowledge. In sequential data assimilation, it is conditioned on previous data and the prediction of a simulation. Let $y^{1:n}$ denote all observations up to time step n . Given a distribution $p(x^{n-1}|y^{1:n-1})$, the prior, or predictive, distribution $p(x^n|y^{1:n-1})$ conditioned on all data from previous time steps is given by

$$p(x^n|y^{1:n-1}) = \int p(x^n|x^{n-1})p(x^{n-1}|y^{1:n-1}) dx^{n-1}, \quad (4)$$

where $p(x^n|x^{n-1})$ is the probability density determined by the transition function from Equation (1). With that prior, Bayes' formula for sequential data assimilation becomes

$$p(x^n|y^{1:n}) = \frac{p(y^n|x^n)p(x^n|y^{1:n-1})}{p(y^n|y^{1:n-1})}, \quad (5)$$

with $p(x^0)$ fixed to represent the initial knowledge of the system before any measurements.

Since we always incorporate available measurements, we simplify the notation by defining the distributions at time step n to be implicitly conditioned on measurements from the previous time steps. We define $p(x^n) \equiv p(x^n|y^{1:n-1})$ and $p(x^n|y^n) \equiv p(x^n|y^{1:n})$. That also allows us to drop the time step superscript when looking at data at a single time step. The form of data assimilation in Equations (4) and (5) can be written as two repeated phases, shown both in Algorithm 1 and here mathematically as

$$\text{predict: } p(x^n) = \int p(x^n|x^{n-1})p(x^{n-1}|y^{n-1}) dx^{n-1}, \quad (6)$$

$$\text{update: } p(x^n|y^n) \equiv p(x|y) = \frac{p(y|x)p(x)}{p(y)}, \quad (7)$$

with implicit n superscripts in the update phase. The predict phase advances the distribution $p(x^{n-1}|y^{n-1})$ to $p(x^n)$ using the transition function from Equation (1). The update phase updates the prior $p(x^n)$ to the posterior $p(x^n|y^n)$ using the likelihood $p(y^n|x^n)$, which is based on the observation function from Equation (2). In Section 2.2, we explain the update phase for the Kalman filter and the EnKF. In Sections 2.3 and 2.4, we introduce the transition and observation operators we use with the EnKF.

2.2 Kalman filters

The standard *Kalman filter* (KF) [37] is a sequential application of Bayes' rule that assumes each distribution is Gaussian in the state x . Consider linear transition and observation functions with Gaussian noise, written as

$$x^{n+1} = f(x^n, \eta_f) = Fx^n + \eta_f \quad \text{and} \quad (8)$$

$$y^{n+1} = h(x^{n+1}, \eta_h) = Hx^{n+1} + \eta_h, \quad (9)$$

where F and H are linear operators; Q and R are the known noise covariances; $\mathcal{N}(\mu, B)$ denotes a multivariate Gaussian distribution with mean μ and covariance B ; $\eta_f \sim \mathcal{N}(0, Q)$; and $\eta_h \sim \mathcal{N}(0, R)$.

In this linear case, an input Gaussian distribution $p(x^{n-1}|y^{n-1})$ always transforms to a Gaussian prior $p(x^n)$ and posterior $p(x^n|y^n)$. If we parametrize the distribution with μ and B as $p(x) = \mathcal{N}(\mu, B)$, then we have linear solutions for Equations (6) and (7). For the linear transition function of Equation (8) where the distribution at the previous time step $n - 1$ is known as $p(x^{n-1}|y^{n-1}) = \mathcal{N}(\mu_a^{n-1}, B_a^{n-1})$, then the predicted (or *forecasted*), distribution is $p(x^n) = \mathcal{N}(\mu_f^n, B_f^n)$, where

$$\mu_f^n = f(\mu_a^{n-1}) \text{ and } B_f^n = FB_a^{n-1}F^T + Q, \quad (10)$$

In the update phase, the KF computes the posterior $p(x^n|y^n)$ given the prior $p(x^n)$, the likelihood $p(y^n|x^n)$, and the observation y^n . For the linear observation function of Equation (9), the likelihood is $p(y|x) = \mathcal{N}(Hx, R)$. Let $\mu_0 = \mu_f^n$ and $B_0 = B_f^n$ be the forecasted mean and covariance of $x_0 = x^n$ from the prediction step. Then the posterior distribution is $p(x|y) = \mathcal{N}(\mu, B)$, where the moments can be calculated as

$$\mu = \mu_0 + K(y - h(\mu_0)) \text{ and} \quad (11)$$

$$B = (I - KH)B_0, \quad (12)$$

with K known as the Kalman gain matrix,

$$K = B_0H^T(HB_0H^T + R)^{-1}. \quad (13)$$

The Kalman gain matrix can be expressed in terms of the covariance of the predicted $x_0 \sim p(x_0)$ and $y_0 \sim p(y|x_0)$. Recall the definition of the covariance $\text{cov}(\cdot)$ and the cross-covariance $\text{cov}(\cdot, \cdot)$ as the expectation of the outer product of the deviations from the mean,

$$B_0 = \text{cov}(x_0) = \mathbb{E}_{x_0 \sim p(x_0)} (x_0 - \mu_0)(x_0 - \mu_0)^T. \quad (14)$$

Then B_0H^T is the cross-covariance $\text{cov}(x_0, y_0)$, and $HB_0H^T + R$ is the forecast observation covariance $\text{cov}(y_0)$. Thus, K can be expressed as

$$K = \text{cov}(x_0, y_0) \text{cov}(y_0)^{-1}. \quad (15)$$

This is equivalent to Equation (13) in the Gaussian case, but it can be easily extended to non-Gaussians, for instance, in the EnKF.

There are several KF variants based on Equations (10) to (13) made to deal with invalid assumptions in the standard KF. Specifically, they are made to handle nonlinearity (and therefore, non-Gaussianity) and the inability to store the full covariance matrix. Below, we explain three methods to handle nonlinearity to show how the EnKF method uses an ensemble to avoid storing large matrices.

The *extended Kalman filter* (EKF) (first described by Smith *et al.* [38]) extends Equations (10) to (13) to nonlinear transitions and observations by linearizing the functions about the prior mean. H is replaced by the Jacobian $\frac{dh}{dx}$ evaluated at $x = \mu_0$ and similarly for $F = \frac{df}{dx}$. The pseudocode for the predict and update phases is shown in Algorithm 2. Since EKF linearizes the transition and observation operators, it fails when the system exhibits significant nonlinear behavior when transitioning between observation time steps or between the prior mean and the posterior mean. Similarly to the original KF, the EKF can also fail when the noise statistics are specified incorrectly, as described by Valappil and Georgakis [39].

The *iterated extended Kalman filter* (IEKF) extends the EKF by taking smaller steps in time and in posterior updates. It repeats Equation (10) a fixed number of times with a smaller time step size, correspondingly smaller Q , and a recomputed linearization F at each iteration. Similarly, Equations (11) to (13) are iterated a fixed number of times with a scaled-up observation error covariance R and a recomputed linearization H at each iteration's computed mean. This can be computationally expensive, but reduces linearization errors for nonlinear problems compared to the EKF.

The *ensemble Kalman filter* (EnKF) [40], [41] handles non-linearity by using multiple values of the operators at different points, which can be contrasted with the EKF strategy of using the Jacobian at the mean. The prior is represented by an ensemble of samples. The predict phase advances each sample forward in time using the transition operator. The update phase simulates observations of each sample and applies a linear Bayesian update to each sample to better match the true observations. The update assumes the state and observation samples are jointly Gaussian, so this method is optimal only for the linear KF case. However, because the samples do not have to be Gaussian, this method has the capability of expressing non-Gaussian distributions. Specifically, if the transition operator is nonlinear, the prior $p(x)$ for the update step is not Gaussian, and if h is nonlinear, the likelihood $p(y|x)$ for the update step is not Gaussian.

Algorithm 2: Extended Kalman filter implementation for use with Algorithm 1

Input: forward physics operator $f(x; t_0, t)$ that simulates x from time t_0 to time t with noise covariance matrix Q , measurement operator $h(x)$ with noise covariance matrix R

```

1 Function Predict( $(\mu_0, B_0), t_0, t$ ):
   // Equation (10)
2    $\mu \leftarrow f(\mu_0; t_0, t)$ 
3    $F \leftarrow \frac{df}{dx}(\mu_0)$ 
4    $B \leftarrow FB_0F^T + Q$ 
5   return  $(\mu, B)$ 

6 Function Update( $(\mu_0, B_0), y$ ):
7    $H \leftarrow \frac{dh}{dx}(\mu_0)$ 
   // Equation (13)
8    $K \leftarrow B_0H^T(HB_0H^T + R)^{-1}$ 
   // Equation (11)
9    $\mu \leftarrow \mu_0 + K(y - h(\mu_0))$ 
   // Equation (12)
10   $B \leftarrow (I - KH)B_0(I - KH)^T + KRK^T$ 
11  return  $(\mu, B)$ 

```

The Kalman update in Equations (11) to (13) is equivalent to taking the mean of a linear transform z in the form $z(x, y) = x + K(y - Hx - \eta_h) = (I - KH)x + K(y - \eta_h)$. If x is sampled from $\mathcal{N}(\mu_0, B_0)$, the resulting z is distributed according to the posterior $\mathcal{N}(\mu, B)$. Thus, we have a method of computing posterior samples based on prior samples and measurements.

Let the ensemble be forecasted samples $x_{f,i}$ indexed by i from 1 to N_e . They can be described as samples of $\mathcal{N}(\mu_0, B_0)$ with forecasted sample mean $\mu_0 = \sum x_{f,i}/N_e$ and sample covariance $B_0 = X_f X_f^T$, where X_f is a matrix where the i -th column is $(x_{f,i} - \mu_0)/\sqrt{N_e - 1}$. Equation (11) applies to each sample to update the samples with the observation y , written as

$$x_{a,i} = x_{f,i} + K(y - y_{f,i}) \text{ for } i \in \{1, 2, \dots, N_e\}, \quad (16)$$

where $y_{f,i} = h(x_{f,i}, \eta_{h,i})$ is a simulated observation, $\eta_{h,i}$ is a sample of the noise for the observation operator, and $x_{a,i}$ is a sample of the posterior. Note that the observation operator here on each sample is simulated with noise, whereas in Equation (11), the mean is observed without noise, since the noise is assumed to have zero mean. The EKF uses Equation (13) to compute the Kalman matrix K with a linearized form of h . Directly plugging in $B_0 = X_f X_f^T$ yields

$$K = X_f (H X_f)^T ((H X_f)(H X_f)^T + R)^{-1}. \quad (17)$$

For the EKF, H is the Jacobian of h at $x = \mu_0$, and it is used to estimate how differences in the value of x correspond to differences in y . However, for nonlinear functions, this may poorly describe the behavior of h in a larger neighborhood around μ_0 . Instead, the EnKF better explores the nonlinearity of the function by sampling those differences at various points, using the approximation $H(x_{f,i} - \mu_0) \approx y_{f,i} - \mu_y$, where $\mu_y = \sum_j y_{f,j}/N_e$ is the mean of the predicted observations. This approximation yields the version of the Kalman matrix shown in Equation (15). Let $B_y = Y_f Y_f^T$ be the sample observation covariance, where Y_f is a matrix where the i -th column is $(y_{f,i} - \mu_y)/\sqrt{N_e - 1}$. The covariance form of the Kalman matrix removes possibly costly applications of H by replacing the linear approximation $H X_f$ with the difference matrix Y_f , yielding

$$K = X_f Y_f^T (Y_f Y_f^T)^{-1}. \quad (18)$$

Note that if the ensemble size is smaller than the observation size, the sample observation covariance is guaranteed to be singular. If the (non-singular) observation noise covariance R is known, the sample observation covariance can be computed as $\hat{Y}_f \hat{Y}_f^T + R$, where $\hat{Y}_f \hat{Y}_f^T$ is the non-noisy sample observation covariance obtained from simulating observations without noise. Or, a non-singular form of the sample observation covariance can be obtained by adding a small regularization as $Y_f Y_f^T + \epsilon_h R$, where $Y_f Y_f^T$ is the noisy sample observation covariance and ϵ_h is some small constant.

Pseudocode for the EnKF predict and updates phases is shown in Algorithm 3.

The Kalman filter update in Equation (11) can be thought of as solving the linearized optimization problem

$$\mu = \arg \min_x \|h(\mu_0) + H(x - \mu_0) - y\|_{R^{-1}}^2 + \|x - \mu_0\|_{B_0^{-1}}^2, \quad (19)$$

and then the covariance estimate B is the inverse Hessian of the optimization objective at μ . Similarly, the EnKF can be thought of as updating each ensemble member by solving the linearized optimization problem

$$c_i = \arg \min_{c \in \mathbb{R}^{N_e}} \|\mu_y + Y_f c - y\|_{R^{-1}}^2 + \|\mu_0 + X_f c - x_{f,i}\|_{B_0^{-1}}^2, \quad (20)$$

with $x_{a,i} = \mu_0 + X_f c_i$. Compared to the extended Kalman filter, the EnKF must do multiple linear solves to apply the Kalman gain matrix to each ensemble member, but the EnKF gains the benefit of the covariance matrix being implicitly represented and implicitly updated.

Although the EnKF efficiently represents the covariance, the EnKF encounters similar challenges as other variants of the KF, specifically in choosing noise statistics. When noise statistics are underestimated, the filter's estimated state covariance becomes increasingly small, such that new observations have negligible effect on the estimated state and the filter diverges from the truth. This is especially an issue for the EnKF with small sample size. Note that the update to each x resides in the range of X , so it is important that X have full column rank, requiring the ensemble members to stay separated.

To manage this filter divergence, a conventional approach is to increase the variance in the state. Covariance inflation, described by Anderson and Anderson [42], artificially inflates the covariance of the ensemble by an ad hoc factor. Hamill and Snyder [43], Whitaker and Hamill [44], and Whitaker *et al.* [45] showed that this simple, efficient approach improved the predictive accuracy of atmospheric data assimilation models. In the context of seismic measurements, Alfonzo and Oliver [24] increased the state covariance by estimating observation noise using observation error, thereby avoiding filter divergence.

Filter divergence is especially a problem when observations are assimilated often. For seismic surveys, we assume observations are expensive and therefore temporally sparse, and we do not assimilate enough observations to encounter filter divergence. Our EnKF simulates reservoir dynamics for a year with unknown permeability and then assimilates a seismic survey. The uncertainty in the parameters governing the reservoir dynamics over this large of a time period is enough to ensure the filter covariance does not become too small. The next two subsections describe the reservoir dynamics and the seismic observation operator we use for the EnKF.

2.3 Two-phase flow

Multi-phase porous flow is a standard approximation for CO₂ reservoir dynamics. For our purposes, the reservoir consists of briny water and injected supercritical CO₂ flowing through porous rock. Simulations may also account for aqueous CO₂, but in our experiments, we consider the two fluids to be immiscible.

For each fluid, a saturation field describes what proportion of the pore space is filled with that fluid. Due to differences in the fluids' adhesion to the rock, each fluid has its own pressure field, although in our experiments, we take the pressure fields to be identical. Let S_g and P_g be the CO₂ saturation and pressure, usually written with no subscript because they are the main quantities of interest. For two-phase flow, the water saturation S_w and pressure P_w can be directly computed as $S_w = 1 - S_g$ and $P_w = P_g + P_c$, where P_c is the capillary pressure. Capillary pressure can be a complex function [46], but we do not attempt to address that field of research. Instead, we focus on the effects of permeability and take capillary pressure to be 0.

The governing PDE is the mass balance equation with Darcy flow,

$$\frac{\partial(\phi \rho_i S_i)}{\partial t} - \nabla \cdot (\rho_i v_i) = \rho_i q_i, \quad (21)$$

$$v_i = -k_{r,i} / \mu_i K \nabla (P_i - \rho_i g Z), \quad (22)$$

$$S_i, P_i \text{ given at } t = 0, \quad (23)$$

with g being gravitational acceleration and Z being depth. Fluid i has fluid density ρ_i , velocity v_i , volume injection rate q_i , relative permeability $k_{r,i}$, and fluid viscosity μ_i . The permeability field K describes the relationship between fluid flow rate and an applied pressure gradient. The flow rate is slowed by viscosity and relative permeability. Permeability is usually expressed in millidarcies and is anisotropic, typically favoring horizontal directions due to sedimentary layering. We represent it with a diagonal tensor separated into vertical and horizontal components,

$$K = \begin{bmatrix} K_v & 0 \\ 0 & K_h \end{bmatrix}, \quad (24)$$

Algorithm 3: Ensemble Kalman filter implementation for use with Algorithm 1

Input: forward physics operator $f(x, \eta_f; t_0, t)$ that simulates x from time t_0 to time t with noise distribution $p(\eta_f)$, measurement operator $h(x, \eta_h)$ with noise distribution $p(\eta_h)$ with estimated covariance R

```

1 Function Predict( $\{x_1, x_2, \dots, x_{N_e}\}, t_0, t$ ):
2   for  $i$  in  $\{1, 2, \dots, N_e\}$  do
3     Sample  $\eta_f \sim p(\eta_f)$ 
4      $x_i \leftarrow f(x_i, \eta_f; t_0, t)$ 
5   return  $\{x_1, x_2, \dots, x_{N_e}\}$ 

6 Function Update( $\{x_1, x_2, \dots, x_{N_e}\}, y$ ):
7   for  $i$  in  $\{1, 2, \dots, N_e\}$  do
8     Sample  $\eta_h \sim p(\eta_h)$ 
9      $y_i \leftarrow h(x_i, \eta_h)$ 
10   $\mu_x \leftarrow \sum_{i=1}^{N_e} x_i / N_e$ 
11   $\mu_y \leftarrow \sum_{i=1}^{N_e} y_i / N_e$ 
12  for  $i$  in  $\{1, 2, \dots, N_e\}$  do
13     $X_f[:, i] \leftarrow (x_i - \mu_x) / \sqrt{N_e - 1}$ 
14     $Y_f[:, i] \leftarrow (y_i - \mu_y) / \sqrt{N_e - 1}$ 
15   $K \leftarrow X_f Y_f^T (Y_f Y_f^T + R)^{-1}$ 
16  for  $i$  in  $\{1, 2, \dots, N_e\}$  do
17     $x_i \leftarrow x_i + K(y - y_i)$ 
18  return  $\{x_1, x_2, \dots, x_{N_e}\}$ 

```

with K_h being a heterogeneous field of the horizontal permeability and K_v/K_h being a constant less than 1. The porosity ϕ is a field with values in the range 0–1 representing how much of the rock is accessible by the fluids (typically about 20%). The relative permeability is a nonlinear function of the saturation. In line with existing literature, we use a modified Brooks-Corey model with residual saturation α for both CO₂ and brine, given by

$$k_{ri} = \text{clamp}((1 - 2\alpha)^{-1}(S_i - \alpha), 0, 1)^2 \quad (25)$$

$$= \begin{cases} 1 & \text{if } S_i \geq 1 - \alpha \\ 0 & \text{if } S_i \leq \alpha \\ (1 - 2\alpha)^{-2}(S_i - \alpha)^2 & \text{else} \end{cases}. \quad (26)$$

Let \mathcal{M} solve the PDE from time t_n to t_{n+1} with initial conditions S^n and P^n , permeability K , and porosity ϕ , written as

$$S^{n+1}, P^{n+1} = \mathcal{M}(S^n, P^n, K, \phi; t_n, t_{n+1}). \quad (27)$$

The resulting saturation is then used to simulate seismic measurements, as described in the next subsection.

2.4 Seismic observation

Surface-seismic data allows measuring subsurface changes without drilling wells. In active-source surface seismic, a seismic source, such as an explosive or air gun, on the surface sends seismic waves into the reservoir. Spatial differences in subsurface wave velocity cause the waves to be reflected or transmitted back to receivers on the surface. The data recorded for this measurement consists of a time series for each possible source-receiver pair.

The wave dynamics are governed by the wave equation. To simulate seismic measurements, the wave equation must be solved for each source to determine the data collected at the receiver locations. In terms of the acoustic pressure field δ_p , the governing wave dynamics are

$$\frac{m}{\rho} \frac{\partial^2 \delta_p}{\partial t^2} - \nabla \cdot \left(\frac{1}{\rho} \nabla \delta_p \right) + w \frac{\partial \delta_p}{\partial t} = \frac{q}{\rho}, \quad (28)$$

where m is the P-wave squared slowness field, ρ is the density field, w is a spatially-varying dampening parameter that is nonzero only in the absorbing boundary layer, and q is an acoustic source. The boundary layer is used to simulate

an infinite domain, ensuring any waves that would escape the system of interest are absorbed by the boundary instead of being reflected back into the system.

Seismic measurements can detect CO₂ because the density and squared slowness at each point is dependent on the material composition at that point, including the rock composition and the relative concentrations of CO₂ and brine. This relation is specified by a rock physics model, and a typical rock physics model for CO₂ reservoirs is the patchy-saturation model. Past research has investigated the effects of pressure in the rock physics model [47], [48], but we neglect that here to focus on the leading order effect. The patchy-saturation rock physics model, described in Chapter 1 of [49], expresses the density and squared slowness as a pointwise function of the CO₂ saturation and a baseline model representing the density and squared slowness before injection. This model is a nonlinear interpolation of the squared slowness with 0% CO₂ and 100% CO₂ in the pore space, based on the P-wave modulus of the rock and fluids.

The P-wave modulus λ is related to the density and squared slowness by $\lambda = \rho/m$, and the shear wave modulus G is related to the density and shear wave squared slowness m_G by $G = \rho/m_G$. We use a typical relation of $m_G = 3m$, but in general, the relation can be more complex. The bulk modulus B is related to the P-wave and shear wave moduli by $B = \lambda - 4/3G$.

Gassman's equation for porous media describes the relation between composite bulk moduli and constituent bulk moduli based on porosity [50]. Here, the constituent bulk moduli are B_0 for the mineral making up the porous rock, B_w for water, and B_g for CO₂. Given the density and velocity before injection, the bulk modulus $B_{wr} = \frac{5}{9}\rho/m$ of the pre-injection brine-rock system is computed using the relations $B_{wr} = \lambda_{wr} - 4/3G$, $m_G = 3m$. Then Gassman's equation below can be solved for the bulk modulus B_{gr} of the rock fully saturated with CO₂,

$$\frac{\phi^{-1}B_w}{B_0 - B_w} - \frac{B_{wr}}{B_0 - B_{wr}} = \frac{\phi^{-1}B_g}{B_0 - B_g} - \frac{B_{gr}}{B_0 - B_{gr}}. \quad (29)$$

Replacing brine with CO₂ does not change the shear modulus, so the resulting P-wave modulus of rock saturated with CO₂ is $\lambda_{gr} = B_{gr} + 4/3G$.

The patchy-saturation model uses an arithmetic average for the density and a harmonic average for the P-wave modulus,

$$\rho(S; \rho_{wr}) = \rho_{wr} + S\phi(\rho_g - \rho_w), \quad (30)$$

$$\lambda(S; \lambda_{wr}) = [(1 - S)\lambda_{wr}^{-1} + S\lambda_{gr}^{-1}]^{-1}, \quad (31)$$

where $\lambda_{wr} = \rho_{wr}/m$ with pre-injection density ρ_{wr} and squared slowness m_{wr} . The harmonic average is a result of assuming the pressure is equalized in the mixed fluid. Increasing the CO₂ saturation decreases the density and tends to decrease the P-wave modulus, depending on porosity. The squared slowness is a quadratic function of the saturation,

$$\begin{aligned} m(S; \rho_{wr}, m_{wr}) &= \rho(S)/\lambda(S) \\ &= [\rho_{wr} + S\phi(\rho_g - \rho_w)] [(1 - S)\lambda_{wr}^{-1} + S\lambda_{gr}^{-1}]. \end{aligned} \quad (32)$$

Given a squared slowness field m from the rock physics model, let $d = \mathcal{H}(m, \rho) + \eta$ be the waveforms representing simulating the seismic waves and obtaining measurements at the receivers with noise η . In terms of the CO₂ saturation S ,

$$d(S; \eta) = \mathcal{H}(m(S), \rho(S)) + \eta, \quad (33)$$

where d being a vector with components $d_{ij}(t)$ as the acoustic pressure measurement at receiver i from source j at time t . These are the full-waveform measurements we use for the EnKF.

3 EnKF applied to CO₂ plume with seismic observations

We apply the scalable, efficient EnKF to the two-phase flow system with seismic observations and show that it gives good estimates of the CO₂ saturation in a high-dimensional (high-resolution) system with temporally sparse seismic measurements. As our seismic model does not depend on the CO₂ pressure, we focus solely on estimating the CO₂ saturation over time. We improve upon the existing literature by addressing all three issues of (1) relatively large problem size with (2) CO₂ dynamics and (3) seismic data. Details on the transition and observation operators are below.

3.1 Transition operator

We use Equation (27) as the transition operator. The permeability and porosity fields cannot be known exactly, which must be accounted for in our EnKF. We focus on the uncertainty created by the unknown permeability field, and we assume the porosity field is known to be a constant 25%. Accounting for the uncertainty in the permeability amounts to initializing each ensemble member with a different realization of the permeability field, with each ensemble member's permeability field fixed across time.

We assume that knowledge of the permeability is represented as a distribution from which we can sample permeability fields. We use a probabilistic relation based on [51] to generate permeability values from velocity values. Specifically, we generate the permeability $K(\mathbf{r})$ at spatial coordinate \mathbf{r} as a pointwise random function of a given velocity field $v(\mathbf{r})$ using

$$K = \begin{cases} 10^{-2}e^{v-3.5} & \text{if } v < 3.6 \\ 10^{-4(3.85-v)}c^{2(v-3.35)} & \text{if } 3.6 \leq v < 3.85 \\ ce^{v-3.7-w} & \text{if } v \geq 3.85 \end{cases} \quad (34)$$

where K is in millidarcies, v is in km/s, and c and w are random fields representing random coefficients for the relation defined in [51]. Specifically, c is a Gaussian random field, fixed across all ensemble samples, with mean 1200, standard deviation 3000, and a Gaussian covariance kernel with length scale 62.5 meters in the horizontal direction and 31.25 meters in the vertical direction. The pointwise random field w is generated from a discrete uniform distribution between 0 and 1.4 with step size of 0.1. The ground-truth permeability is generated via the same methodology with the standard deviation of c replaced with 5.

We assume to know all the transition function parameters except for the saturation, pressure, and permeability. Therefore, an ensemble member's state x^n can be represented by a tuple $x^n = (S^n, P^n, K)$. The transition function f updates the saturation and pressure given the permeability and leaves the permeability unchanged. Using \mathcal{M} described by Equation (27), the transition operator can be written as

$$x^{n+1} = f(x^n) = (\mathcal{M}(S^n, P^n, K, \phi; t_n, t_{n+1}), K). \quad (35)$$

There is no stochasticity in this system, so we drop the η_f term from Equation (1).

Discretization and solution We use the JutulDarcy simulator [52] for this two-phase flow system. JutulDarcy is implemented in the Jutul framework [53], which discretizes spatial fields with finite volumes, discretizes time with an implicit Euler step, and chooses time step sizes automatically with an adaptive time stepper. Jutul solves the discretized system with Newton's method with the necessary Jacobian obtained via automatic differentiation.

3.2 Observation operator

The wave dynamics for the seismic operator take place on a time scale up to a few seconds with a resolution on the order of milliseconds. Changes in the CO₂ saturation occur on a much longer time scale, so we consider the saturation field to be static when simulating seismic measurements.

In line with typical seismic imaging techniques, we construct an approximation of the true pre-injection baseline parameters m_B and ρ_B as a smooth baseline model m_0 and ρ_0 , subtract off the initial seismic measurement, and apply the adjoint Jacobian and a post-processor to obtain a seismic image A as

$$J_0 = \frac{d\mathcal{H}}{dm_0}(m_0, \rho_0), \quad (36)$$

$$h(x, \nu\eta) = PJ_0^T \left(\mathcal{H}(m(S), \rho(S)) + \nu\eta \right), \quad (37)$$

$$h_B(\nu_B^* \eta_B^*) = PJ_0^T \left(\mathcal{H}(m_B, \rho_B) + \nu_B^* \eta_B^* \right), \quad (38)$$

$$A(x, \nu\eta, \nu_B^* \eta_B^*) = h(x, \nu\eta) - h_B(\nu_B^* \eta_B^*), \quad (39)$$

where the measurements depend only on the saturation of the state tuple $x = (S, P, K)$; ν and ν_B^* control the noise magnitude of the simulation and the true observations, respectively; and the post-processor operator P mutes the water layer and scales the image as a function of depth as suggested by Herrmann *et al.* [54]. Note that the image A is a constant offset from the observation operator h , so it makes no difference in the filter whether we use h or A as the observation.

Each frequency component of the noise is drawn from a zero-centered normal distribution with standard deviation proportional to the corresponding frequency’s contribution to the source Ricker wavelet. We calibrate the noise norm in terms of the signal-to-noise ratio (SNR) $\gamma = \nu^{-2}$, typically expressed in decibels as $10 \log \gamma$. We consider the “signal” to be the difference in the observation from the smooth baseline model observation d_0 . We scale the noise η to have the same norm as the signal so that $\nu\eta$ has the signal-to-noise ratio γ ,

$$\gamma = \frac{\|\mathcal{H}(m(S), \rho(S)) - d_0\|^2}{\|\nu\eta\|^2} = \frac{1}{\nu^2}, \quad (40)$$

and similarly for η_B^* , where the norm is defined as $\|\eta\|^2 = \sum_{i,j} \int \eta_{ij}(t)^2 dt$, summed over the sources and receivers and integrated over time.

Linearization The Kalman filter is exact for linear transition and observation operators with additive Gaussian noise. To avoid introducing too much complexity at once to this research, we linearize the seismic operator \mathcal{H} . Thus, we take the initial step of showing that the EnKF accommodates the nonlinearity from the two-phase flow transition and the patchy-saturation model.

The seismic operator can be re-parameterized in terms of squared slowness and impedance as $\mathcal{H}_{mz}(m, z)$. We choose the acoustic impedance $z = \rho/\sqrt{m}$ because the resulting seismic images (computed with inverse scattering imaging conditions) lack low-frequency updates, thereby revealing the shape of the plume better. We linearize this operator \mathcal{H}_{mz} using the Jacobian \hat{J}_0 with respect to the acoustic impedance about the smooth baseline $z_0 = \rho_0/\sqrt{m_0}$. Thus, for the linearized model, we replace $\mathcal{H}(m, \rho)$ in Equations (36) to (40) with

$$\bar{\mathcal{H}}_{mz}(m, z) = \mathcal{H}_{mz}(m_0, z_0) + \hat{J}_0(z - z_0), \quad (41)$$

where the impedance is computed from the patchy-saturation model as

$$z(S; \rho_B, m_B) = \sqrt{\rho(S)\lambda(S)}, \quad (42)$$

so that the observation operator is

$$h(x, \nu\eta) = P\hat{J}_0^T \left(\hat{J}_0(z(S) - z_0) + \nu\eta \right), \quad (43)$$

with ground-truth observation $y = h(x^*, \nu^*\eta^*)$.

Uncertain values Inverting seismic data itself is difficult, so we do not confound that difficulty with extra uncertainty in the rock physics model. Instead, we assume m_B and ρ_B are known exactly for the patchy-saturation model, and we compute the smooth baseline model parameters from a Gaussian blur of m_B and ρ_B .

Discretization and solution We use the JUDI software [55], [56] for this seismic system, which solves the wave equation using the Devito package [57], [58]. The method is an 8th order spatial finite differencing scheme with 2nd order in time with time step size chosen based on the CFL conditions described by Lines *et al.* [59].

3.3 Comparison to other algorithms

For the EnKF, we initialize N_e ensemble members with different permeability models and zero saturation. These states represent possibilities for the state of the reservoir at the initial time. For each ensemble member, we simulate two-phase flow with CO₂ injection until the measurement time. The EnKF uses the ensemble covariance and the measurement covariance to update the saturations of each ensemble member towards a value consistent with the observations, according to Equation (16). Then the simulate-update process is repeated, with the two-phase flow simulation advancing each ensemble member until the next observation time followed by a measurement being incorporated that updates the ensemble states.

The EnKF assimilates data from simulations and observations. In order to be worth the extra computational effort, the EnKF must perform better than similar algorithms that use only data from simulations or only data from observations. We propose a comparison with two baseline ensemble methods of updating the forecast, referred to as no-observations method *NoObs* and a just-observations method *JustObs*. The NoObs method does not incorporate observations; it represents the best prediction we can obtain based on prior physics knowledge, specifically, the two-phase flow model and the probability distribution describing the permeability field. The JustObs method does not use the fluid-flow physics knowledge; it represents the best prediction we can obtain based solely on observations, specifically, waveform observations from Equation (33). The JustObs optimization is ill-posed and can be sensitive to the initial guess for

optimization, so we initialize it with the forecasted ensemble mean and add a regularization term $C(x)$, defined later. The uninitialized and unregularized version performed much worse, and we do not show it. In that sense, JustObs does use the transition physics knowledge, but much less than the EnKF and NoObs methods.

The forecast for each method is computed in the same way. The previous analysis state x_a at time step $n - 1$ for ensemble member i is simply advanced forward in time with the transition operator, written as

$$x_{f,i}^n = f(x_{a,i}^{(n-1)}). \quad (44)$$

We can see the similarities between three methods by writing them each as an optimization, dropping the subscript from x since they are all at time step n :

For NoObs,

$$\begin{aligned} x_{a,i} &= \arg \max_x p(x|x_{f,i}^0) \\ &= \arg \min_x \|x - x_{f,i}\|_{B_0^{-1}}^2. \end{aligned} \quad (45)$$

For JustObs,

$$\begin{aligned} x_{a,i} &= \arg \max_x p(x|y^n) \\ &= \arg \min_x \|h(x) - y^n\|_{R^{-1}}^2 + C(x). \end{aligned} \quad (46)$$

For EnKF,

$$\begin{aligned} x_{a,i} &= \arg \max_x p(x|y^{1:n}) \\ &= \arg \min_x \|\hat{h}(x) - y^n\|_{R^{-1}}^2 + \|x - x_{f,i}\|_{B_0^{-1}}^2. \end{aligned} \quad (47)$$

Recall from Equation (20) that the EnKF uses a linearized observation operator (written $\hat{h}(x)$ here) based on the ensemble members and constrains x to be expressed by the range of the ensemble mean deviations. The version here is simplified to more easily compare to NoObs and JustObs.

Because these are ensemble methods, each ensemble member has a separate realization for $x_{f,i}$ and $x_{a,i}$. Each of the above equations is solved for each ensemble member. Since each ensemble member has a different $x_{f,i}$, the NoObs and EnKF methods include uncertainty in the resulting $x_{a,i}$. The NoObs optimization has a simple solution $x_{a,i} = x_{f,i}$ because the observations are not included. In JustObs, the resulting $x_{a,i}$ is identical for each ensemble member because $x_{f,i}$ does not appear in the optimization expression. For all methods, due to each ensemble member's unique permeability field, the ensemble states tend to drift away from each other and from the ground-truth state when the transition function is applied.

For the JustObs optimization, we use a projected quasi-Newton algorithm with spectral projected gradient algorithm described by Schmidt *et al.* [60] and implemented in Julia by Louboutin *et al.* [61]. For regularization $C(x)$, we use $C(x) = \|\lambda_h^{-1}L_h S\| + \|\lambda_v^{-1}L_v S\|$, with length scales λ_h and λ_v and linear operators L_h and L_v that compute the horizontal and vertical gradients of the saturation field S with finite differences. We experimented with the following norms to regularize the gradient of the saturation: ℓ_1 , known as total variation (TV) regularization [62]; ℓ_2 , known as Tikhonov regularization [63]; and a hybrid ℓ_1/ℓ_2 norm [64] that benefits from the sparsity behavior of the ℓ_1 norm without requiring the ℓ_1 -norm projection. These norms have successfully been used for inverting seismic velocity. A useful albeit simplified characterization of these regularizations is TV yields piecewise-constant solutions, Tikhonov yields smoothly-varying solutions, and the hybrid yields piecewise-smooths solutions. The CO₂ plume should be piecewise-smooth instead of piecewise-constant, so we expect the hybrid regularization to yield better results. Indeed, we empirically find the hybrid performs slightly better, but the optimization with each of these norms gave very poor estimates of CO₂ saturation, with nonzero CO₂ saturation placed across much of the domain even with non-noisy data and perfect velocity models. More work could be done to improve the JustObs algorithm, e.g., based on [65]. However, since the focus of this paper is the EnKF, comparing a simple JustObs algorithm to the simplest EnKF algorithm is reasonable.

3.4 Noise tests

We additionally test a range of values for the parameters for the EnKF while keeping the transition and observation models fixed. We show the EnKF's resiliency to deviations from the ideal parameters, and we provide guidance on how

to choose some parameters. Specifically, the EnKF algorithm has choices for how the noise is handled and estimated, and we are interested in how the accuracy of the EnKF’s state estimate accuracy changes under incorrect assumptions and different ways to handle the noise.

Recall that the Kalman update can be written in terms of covariances, and the EnKF uses sample covariances from the ensemble, denoted here with $\widehat{\text{cov}}$ with observation noise covariance estimate or regularization R ,

$$x_{a,i} = x_{f,i} + \widehat{\text{cov}}(x_f, y_f) (\widehat{\text{cov}}(y_f) + R)^{-1} (y - y_{f,i}). \quad (48)$$

Our seismic data is represented as $y_{f,i} = h(x_{f,i}, \nu\eta_i)$, where the norm of η_i is fixed and ν determines the SNR (expressed as $-20 \log \nu$ dB). If the noise covariance is known precisely, $\widehat{\text{cov}}(y_f)$ should be computed without noise as $\widehat{\text{cov}}(h(x_f, 0))$, and R should fully represent the noise covariance.

However, we don’t generally know the covariance of the noise, so if we instead compute $\widehat{\text{cov}}(y_f)$ with the noise as $\widehat{\text{cov}}(h(x_f, \nu\eta_h))$, then $\widehat{\text{cov}}(y_f)$ implicitly contains an estimate of the noise covariance. Unfortunately, the number of ensemble members is much smaller than the observation size, which makes $\widehat{\text{cov}}(y_f)$ singular. This necessitates regularization in the inversion of the sample observation covariance, in which case, the matrix R is ideally close to the true noise covariance only in the directions that are not already sampled in $\widehat{\text{cov}}(y_f)$.

Typical handling of the regularization simply parametrizes R as a diagonal scaling of the identity, and we follow suit here. The noise variance is proportional to ν^2 , so we parametrize R as $R(\nu, \beta) = \nu^2 \beta^2 I$, with scaling parameter β^2 being the estimate of the average variance of the observation vector’s entries when the SNR is 0 dB. If we have the true observation noise covariance R^* , we would choose $\beta^2 = \text{mean}(\text{diag}(R))$.

For our noise tests, we consider changing the four noise parameters: first, β , which determines the amount of regularization in the inversion of $\widehat{\text{cov}}(y_f)$; then $\alpha \in \{0, 1\}$, a binary value which determines whether to simulate the noise in the estimate of $\widehat{\text{cov}}(y_f)$; and finally, ν and ν^* , which determine the magnitude of the noise in the simulation and the synthetic ground-truth observations. These scalar parameters are shown underlined in the update equation as

$$x_{a,i} = x_{f,i} + \widehat{\text{cov}}(x_f, h(x_f, \underline{\nu}\eta)) \left(\widehat{\text{cov}}(h(x_f, \underline{\alpha}\underline{\nu}\eta)) + \underline{\nu}^2 \underline{\beta}^2 I \right)^{-1} [h(x^*, \underline{\nu}^* \eta^*) - h(x_{f,i}, \underline{\nu}\eta_i)]. \quad (49)$$

We refer to changing β and α as *regularization tests*, changing ν as *simulated noise tests*, and changing ν^* as *true noise tests*, described in more detail below.

Regularization tests The regularization tests measure performance with different values of β and α , keeping $\nu = \nu^*$ fixed. As β is increased, the update to x_k goes to 0, so we expect the EnKF estimates to approach the NoObs estimates. For $\alpha = 1$, the noise is included in the samples for the sample covariance, and β is simply a regularization parameter. For $\alpha = 0$, R should represent the covariance of the noise in the observation operator, and β is chosen to make the resulting variance match the noise covariance on the diagonal.

Simulated noise tests For these tests, we measure performance when the noise estimate $\nu \neq \nu^*$ while keeping β , α , and ν^* fixed. If ν equals the true noise ν^* , then our ensemble’s observation noise variance is an unbiased estimate of the true observation noise variance. When the noise estimate is too high, we expect to regress to the NoObs results, and when the noise estimate is too low, we expect to fit the noisy data too closely. In practice, the true noise variance is not known exactly but can be estimated based on observations and technical specifications of the sensors. These tests show the robustness of the EnKF to mis-calibration of the noise. Note that we consider strictly unbiased (zero-mean) noise. Biased errors typically occur from incorrect forward models, but we do not address those here.

True noise tests Finally, we further show the robustness of the EnKF by measuring performance with different values of the true noise magnitude ν^* . We are especially interested in how the performance decays for larger values of noise. For these tests, we keep $\nu = \nu^*$ and keep β and α fixed.

4 Test scenario

We show the ensemble Kalman filter performance on a synthetic CO₂ injection problem based on the Compass model, which is a synthetic benchmark for seismic full waveform inversion [66]. We simulate the CO₂ injection for 5 years, with new seismic observations every year. The simulation domain is shown in Figure 1, and the scalar simulation parameters are shown in Table 1.

The Compass model is a large 3D model designed to capture the geological complexities of seismic behaviors in real systems. Running simulations with the full model is expensive, so we limit the domain to a 2D slice, shown in Figure 2.

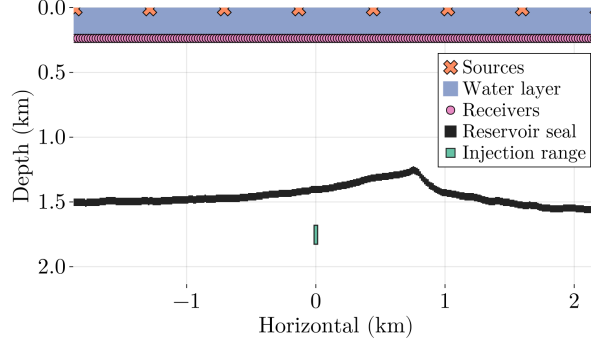


Figure 1: Simulation domain

Domain size	4.05 km × 2.125 km
Grid size	325 × 341
Cell size	12.5 m × 6.25 m

(a) Shared domain parameters.

Simulation length	5 years
Injection depth	1.76 km
Injection extent	37.5 m
Injection rate	0.8 Tg/year
Residual saturation	0.1
K_v/K_h	0.36

(b) Plume parameters.

Simulation length	1.8 s
Source dominant frequency	24 Hz
Source maximum amplitude	7.8 MPa
Signal-to-noise ratio	8 dB
Number of receivers	200
Number of sources	8

(c) Seismic parameters.

Table 1: Simulation parameters

For each ensemble member, the permeability is a function of a deformed version of the true velocity field v . The applied distortion is an elastic deformation provided by the Augmentor.jl software [67]. Let L_i be the domain extent in either the vertical or horizontal direction. The deformation is expressed as a regular coarse grid of displacement vectors sampled uniformly with components between $-L_i$ and L_i and then normalized such that the 2-norm over the grid along each displacement component of the vectors is $0.2L_i$. For a displacement field $\mathbf{d}(\mathbf{r})$, the deformed velocity field is expressed as $v'(\mathbf{r}) = v(\mathbf{r} + \mathbf{d}(\mathbf{x}))$.

The dimensions of the coarse grid are chosen uniformly between 30 and 50, and the distortion vectors along the boundary are set to 0. Furthermore, a Gaussian kernel with length scale between $L_i/15$ and $L_i/25$ is applied to smooth the distortion field. For our grid, the root-mean-squared distortion is 20.3 meters in the horizontal direction and 10.7 meters in the vertical direction. After deforming the velocity field, the resulting permeability field using Equation (34).

Each ensemble member has a different permeability model. To avoid extremely high pressure, we choose the simulated injection depth for each permeability model to be the maximum permeability value in the 120 meter range labeled in Figure 1, and we initialize the saturation field with a random-valued saturation patch of 57 grid cells around that location.

Figure 3 shows the ground truth permeability, an example ensemble member’s permeability, as well as the mean and standard deviation of the 256 permeability samples used for the ensemble. Figure 4 shows the ground-truth saturation and observation at two times.

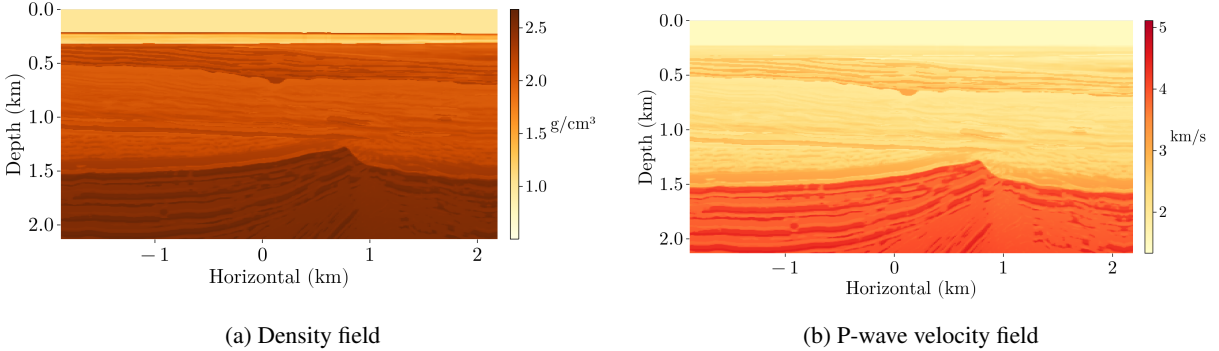


Figure 2: Seismic field parameters. These come from a 2D slice of the compass model.

5 Numerical results

First, we define the metrics we use to measure performance. Since this is a synthetic experiment, we benefit by being able to compare each saturation estimate S directly to the ground truth saturation S^* . The ensemble mean is the standard estimate to show and is the best estimate of the true saturation field in terms of the ℓ_2 norm assuming a Gaussian distribution. Since our transition and observation operators are nonlinear, our distribution is not Gaussian. Still, there is not a clear choice for a different function of the ensemble states to use, so we show the mean and compute error statistics using the mean. We use root-mean squared error (RMSE) defined as

$$\text{RMSE}(S, S^*) = \sqrt{\frac{1}{|\Omega|} \int_{\Omega} (S(\mathbf{r}) - S^*(\mathbf{r}))^2 d\mathbf{r}}, \quad (50)$$

approximated as the mean of the squared error in each grid cell of the simulation domain Ω . We also computed the structural similarity index measure (SSIM) metric defined in [68]. SSIM takes into account edges as well as values and is strongly correlated with how humans perceive similarity between two images. For our tests, we found the SSIM metric to not yield any more information than the RMSE, so we show only RMSE for most plots.

5.1 EnKF compared to baselines

Figure 5 shows a comparison of the final plumes for EnKF and NoObs, and Figure 6 shows the error in the final plumes. While the ground-truth plume has sharp edges due to the sharp edges in the true permeability field, the estimates are smoother due to each ensemble member having different realizations of the permeability field with different locations for the sharp edges. Furthermore, in order of from most smooth to least smooth, we have the NoObs plume, the EnKF prediction, the EnKF analysis, and the ground-truth. This shows that assimilating observations achieves sharper plume estimates, both in forecasting (the EnKF prediction) and filtering (the EnKF analysis).

The most notable differences occur in areas of low permeability in the ground-truth. Specifically, the ground-truth has empty pockets that the CO_2 does not reach due to the low permeability, and the ground-truth CO_2 saturation does not spread out as much. The NoObs estimate misses all except the single pocket at 1.5 km depth, 0.6 km horizontal. The EnKF recovers that pocket and shows signs of the 5 pockets along 1.6 km depth from -0.3 km to 0.3 km horizontal. We note it is very hard to recover these without updating the ensemble members’ permeabilities, as each time the transition operator is applied, CO_2 flows into the pockets for members that have high permeability there.

Furthermore, the estimated states show larger plume boundaries due to the uncertain permeability allowing the CO_2 to spread faster for some permeability samples. The EnKF estimate shows signs of correcting for this, seen by the noisy scatterings of minuscule but nonzero saturations on the edge of the estimate plume. This is due to the EnKF updating the saturation based on seismic data. Saturation updates outside the boundary of the ground-truth plume tend to push the saturation to be small or even negative, which is then clamped to zero.

Figure 7 shows the error for each method over time, with discontinuities when observations are assimilated. The x-axis starts at year 1 when the first observation is assimilated, because, before observations, each method is identical.

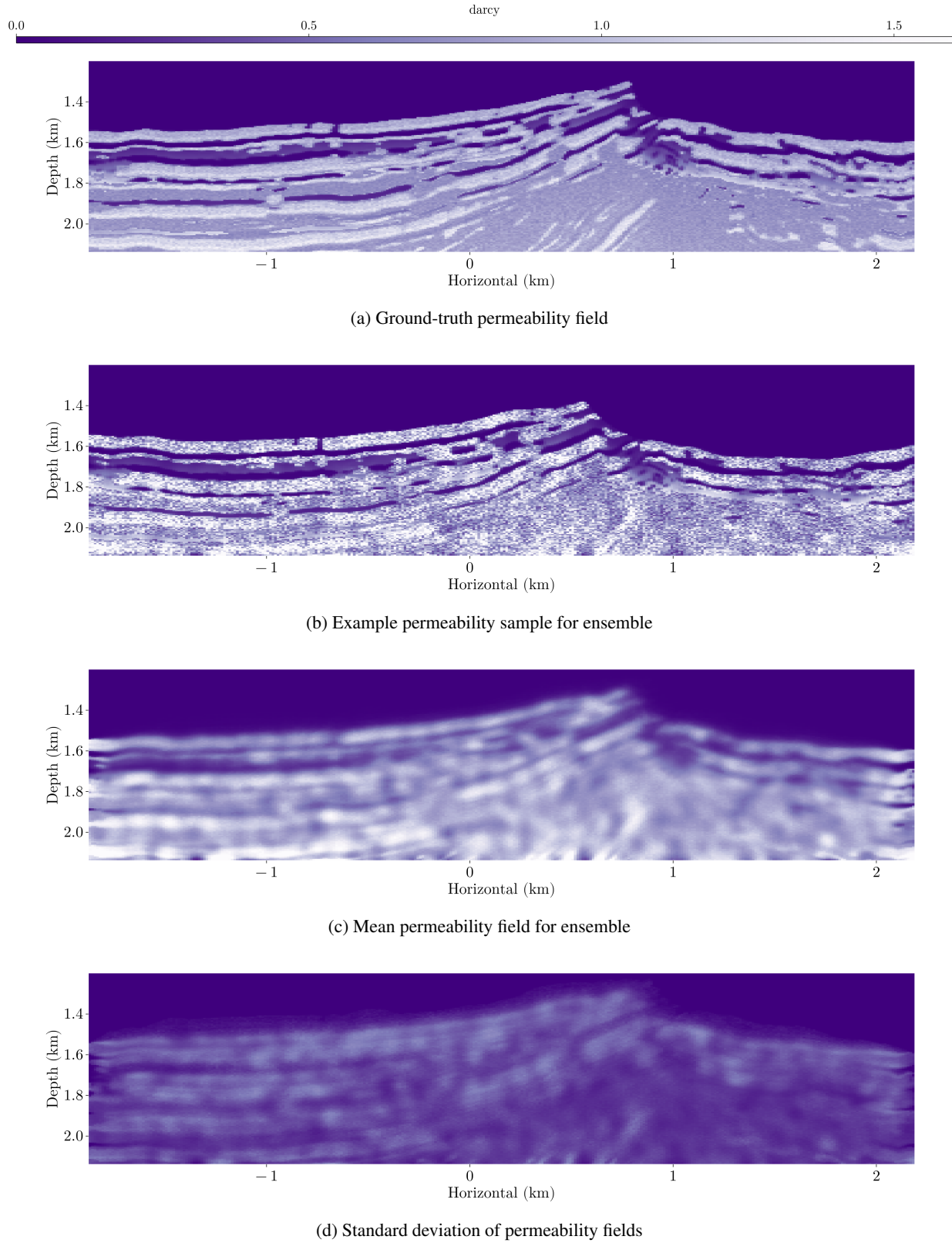


Figure 3: The permeability field is computed from the velocity field with additional perturbations. The ground truth more closely resembles the velocity field, while ensemble permeabilities are much more noisy.

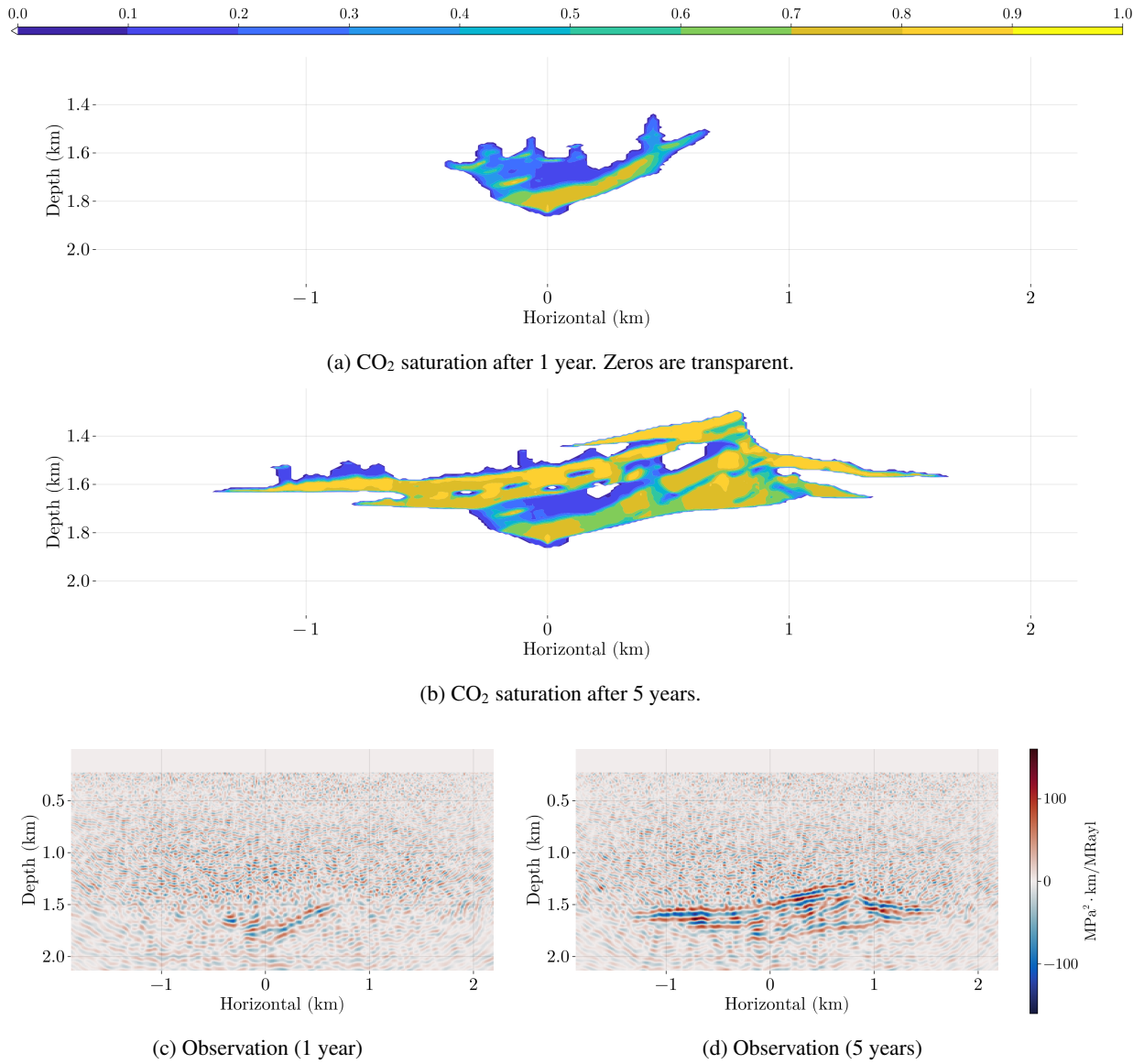


Figure 4: CO₂ plume evolution over time. Observation units for RTM are squared pressure per impedance times depth, with pressure in megapascals, impedance in megarayls ($\text{g}/\text{cm}^3 \cdot \text{km}/\text{s}$), and depth in kilometers.

JustObs was unable to reduce the RMSE with noisy observations, so we show JustObs results solely for non-noisy data. The NoObs error growth over time shows how much the ensemble’s distribution of permeability fields causes the mean estimate to diverge from the ground-truth plume. Comparing the JustObs error with the typically lower NoObs error, we conclude the permeability’s uncertainty in this experiment is small enough that the knowledge of the CO₂ dynamics is more informative than seismic measurements. Real applications may have much higher uncertainty in the CO₂ dynamics, which may make JustObs perform better than NoObs.

The EnKF combines the knowledge of the CO₂ dynamics with the seismic measurements and consistently achieves lower error than NoObs and JustObs, thereby showing the benefit of data assimilation. The uncertainty in the permeability causes a sharp increase in error between observations, which shows a limited ability for making accurate predictions. Future research can use the seismic observations to reduce the uncertainty in the CO₂ dynamics, which will decrease the growth in error between observations.

5.2 EnKF noise parameter tests

By comparing to the baselines, we conclude that the EnKF with our initial choice of EnKF algorithm parameters performs well. Now, we examine performance when modifying the EnKF parameters. Figures 8 to 10 show the results, discussed below, of testing values for the different noise parameters in Equation (49), duplicated here,

$$x_{a,i} = x_{f,i} + \widehat{\text{cov}}(x_f, h(x_f, \underline{\nu}\eta)) \left(\widehat{\text{cov}}(h(x_f, \underline{\alpha}\nu\eta)) + \underline{\nu}^2 \beta^2 I \right)^{-1} [h(x^*, \underline{\nu}^* \eta^*) - h(x_{f,i}, \underline{\nu}\eta_i)]. \quad (49 \text{ revisited})$$

Regularization tests We first vary β with $\nu = \nu^*$ to ensure the EnKF performance is not sensitive to the magnitude of regularization. β scales the regularization covariance $R = \nu^2 \beta^2 I$ in the observation covariance matrix, and has units of MPa²·km/MRayl. If $\alpha = 0$, then R should be the identity scaled by the variance of the noise. By sampling the noise, we form an estimate of the true noise covariance and empirically determine the average noise standard deviation across the seismic observations to be $\nu\beta \approx 11$ for an SNR of 8 dB, which corresponds to $\nu = 10^{-8 \text{ dB}/20} \approx 0.4$ and $\beta \approx 28$. Scaling by the average noise standard deviation is the typical method for regularizing the observation covariance inversion in the EnKF. We additionally compute the largest 256 eigenvalues of the sample estimate of the true noise covariance, as the largest eigenvalue leads to a more unbiased estimate of the regularized observation noise covariance when approximating correlated noise with a multiple of the identity. This leads to an estimate of $\beta \approx 400$.

In Figure 8a, we plot the error as a function of β with simulated noise in the observation covariance ($\alpha = 1$) and determine that a wide range of β values from 10^{-4} to 10^3 achieve equivalent results. The error sharply increases for very small β approximately six orders of magnitude smaller than the true noise standard deviation. As β becomes very large, the post-assimilation error begins to approach the pre-assimilation error as expected. We conclude that if the noise is included in the observation covariance ($\alpha = 1$), then the regularization should be chosen within a couple of orders of magnitude of the true noise standard deviation and err on the side of being smaller.

We then vary β without simulated noise in the observation covariance ($\alpha = 0$) to see if simulating the noise gives the EnKF better performance than fully approximating the noise covariance as a multiple of the identity matrix. In Figure 8b, we plot the error as a function of β . We find that for $\alpha = 0$, the error is much more sensitive to the magnitude of the regularization. Furthermore, we highlight the range of β based on the diagonal of the observation noise sample covariance and the range of β based on the largest eigenvalues. We conclude the minimum error is achieved when choosing the regularization magnitude based on the largest eigenvalues. This can be useful for systems where simulating noise is more costly. For example, the regularization estimate can be computed offline by computing noise samples and the resulting noise covariance eigenvalues.

For full waveform observations, simulating noise is inexpensive compared to the cost of the transition and observation operators, and the robustness in terms of the choice of β parameter when $\alpha = 1$ offsets the low cost of simulating the noise.

Simulated noise tests We then vary ν with ν^* fixed and simulating the observation noise samples ($\alpha = 1$) to ensure the EnKF performance is not sensitive to the estimate of the observation noise magnitude. In Figure 9, we plot the error versus the simulated SNR in decibels, which is $-20 \log_{10} \nu$. As expected, when the estimated noise magnitude is chosen very large (low SNR), the filter approaches the NoObs results, essentially ignoring observations. On the opposite end, when the simulated SNR is too high, the filter puts too much weight on the observations, thus overfitting them and raising the error.

Estimating the noise correctly with estimated SNR = γ^* should give the lowest error in the long term. However, in the short term, a large error in the initial prior can make it advantageous to weight observations higher in earlier time

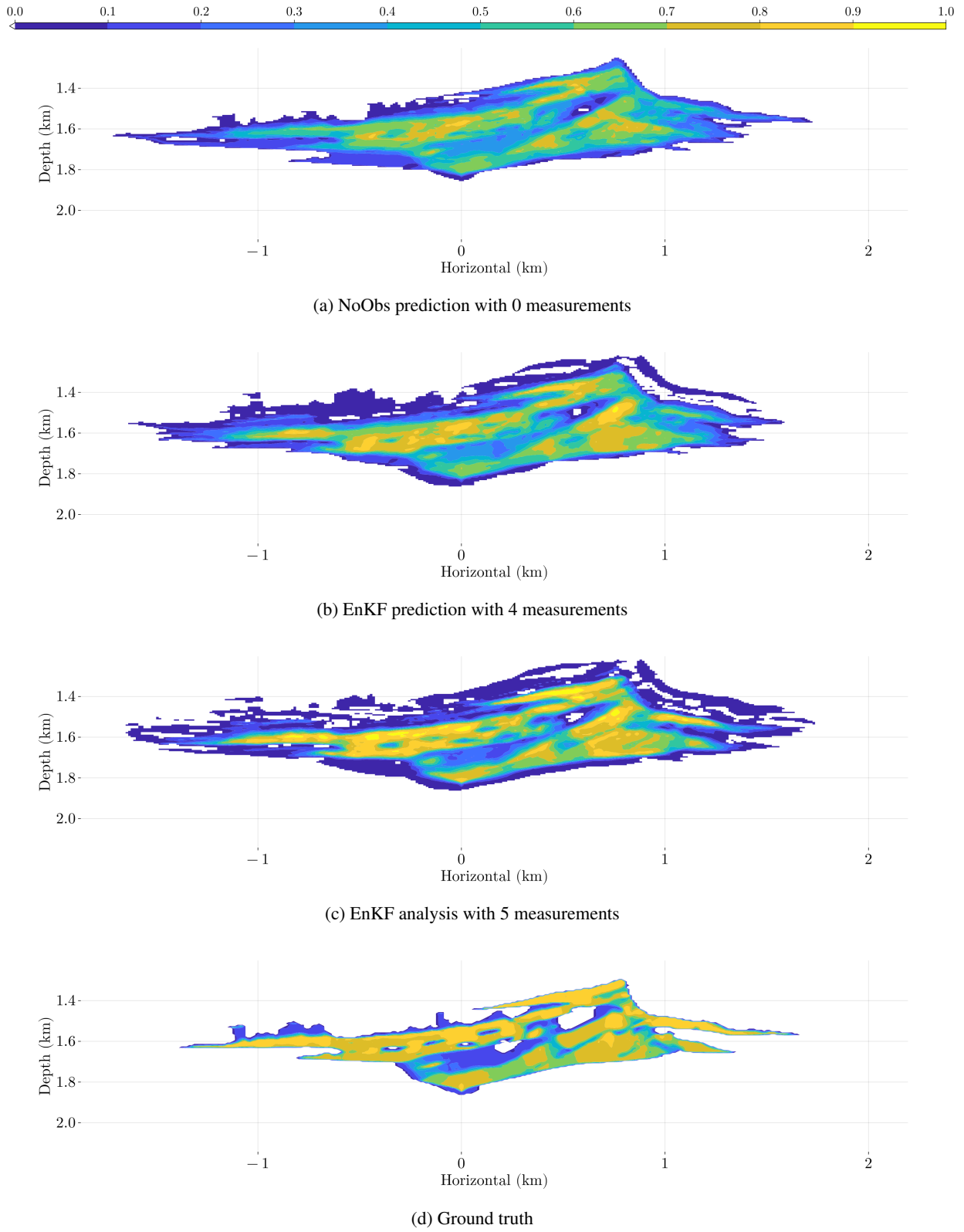
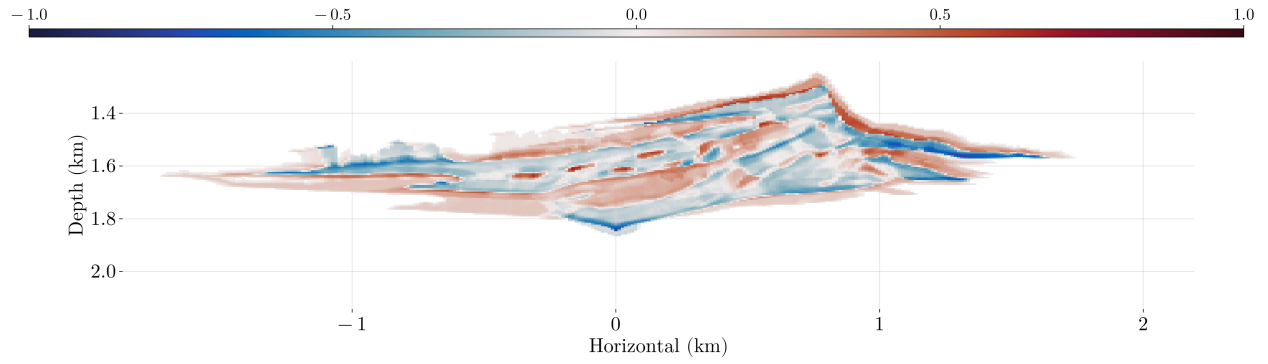
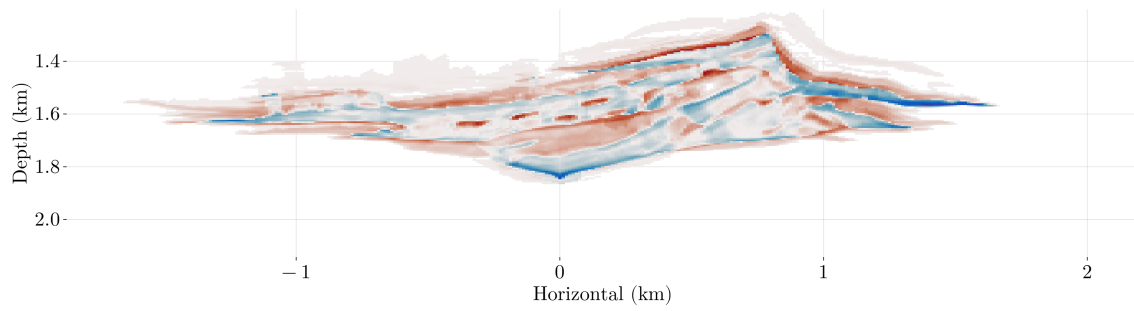


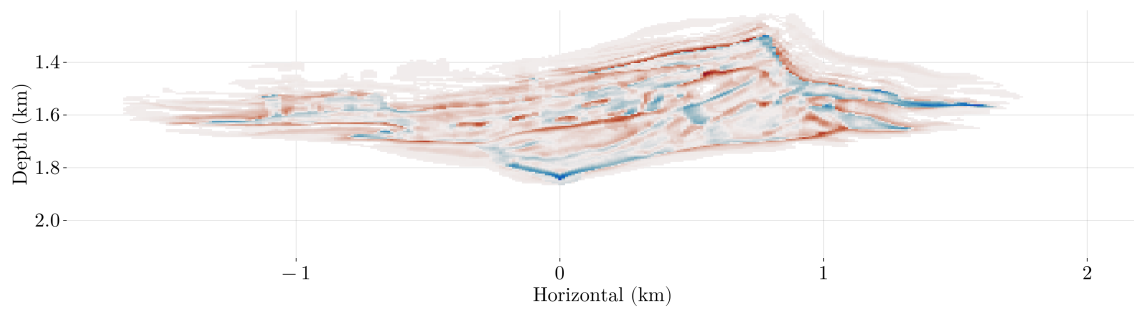
Figure 5: CO₂ saturation after 5 years for NoObs, EnKF, and ground-truth.



(a) NoObs prediction error



(b) EnKF prediction error



(c) EnKF analysis error

Figure 6: CO₂ saturation error after 5 years for NoObs and EnKF.

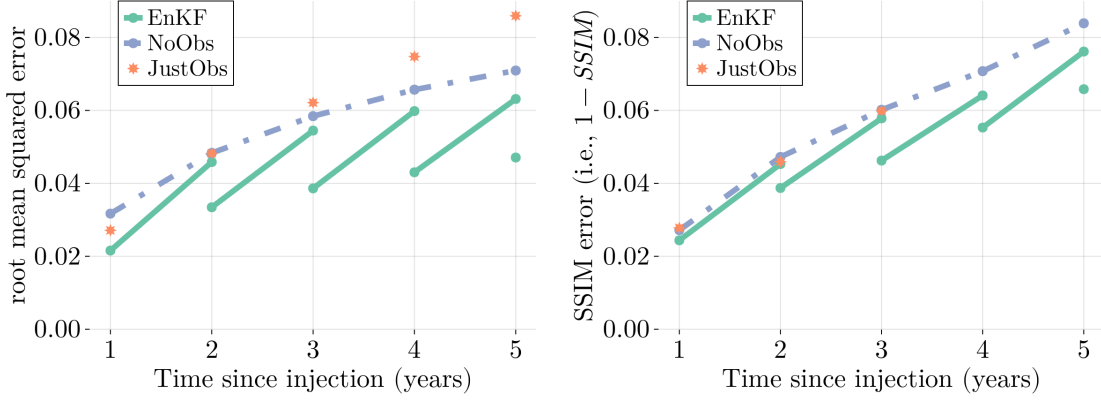


Figure 7: Error in predicted CO₂ saturation over time. The error between observation steps are linearly interpolated. These JustObs errors were generated with non-noisy observations and a hybrid ℓ_1/ℓ_2 regularization, which achieved the lowest error out of the norms we applied. The SSIM error for JustObs is too high to be shown at years 4 and 5.

steps. In Figure 9 at year 1, the minimum RMSE is achieved by overestimating the SNR by 10 dB, but by year 5, the minimum RMSE is achieved by overestimating SNR by 5 dB. As more observations are collected, the effect of the initial prior decreases, and the minimum should shift to coincide with the true SNR γ^* .

True noise tests Finally, we vary ν^* with $\nu = \nu^*$ and simulating the observation noise samples ($\alpha = 1$) to ensure the EnKF can still perform well on varying levels of noisy data. In Figure 10, we plot the error versus the true SNR in decibels. As expected, we find that the EnKF error approaches the NoObs error for large noise magnitudes (low SNR). Except for the first two time steps, we find that the error increases as the noise becomes very small. This can be explained by the results with large SNR in the ν tests in Figure 9 that have large error due to overfitting the noise. As we decrease ν^* and ν together, we see better results, until we reach a point where the $\nu = \nu^*$ does not properly account for the noise. Specifically, for high SNR, we expect simulation error to dominate the noise, and therefore, the error increases. This is not a problem in real scenarios as the real-world seismic noise always dominates floating-point arithmetic errors.

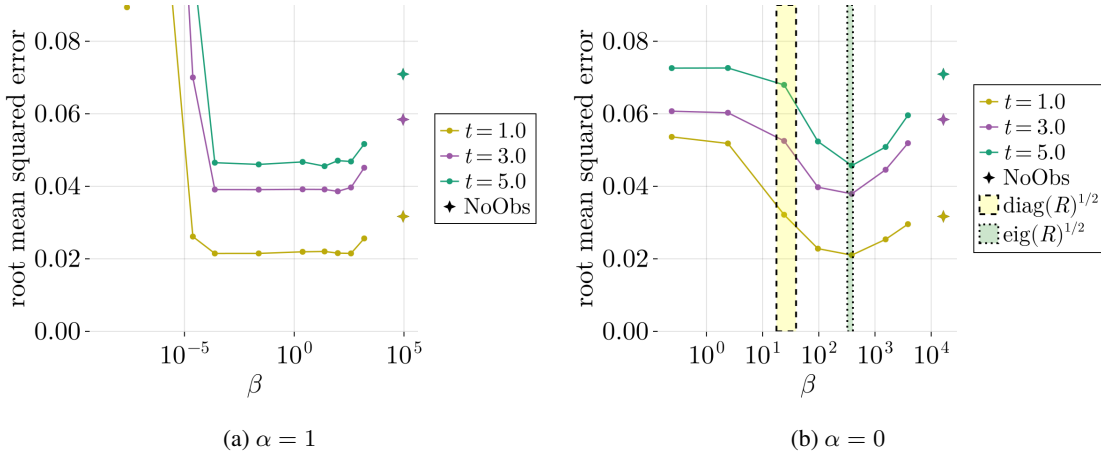


Figure 8: RMSE vs β (MPa² · km/MRayl) with 8 dB SNR ($\nu = \nu^* \approx 0.4$) at three time steps after the EnKF update. In (a), the noise covariance includes simulated noise plus a diagonal identity scaled by β . A wide range of β achieves similar error, with a sharp increase in error for small regularization. In (b), the noise covariance is approximated solely as a diagonal matrix, causing more sensitivity to the choice of β . In either case, the error with large regularization should approach the NoObs case, which is equivalent to $\beta = \infty$.

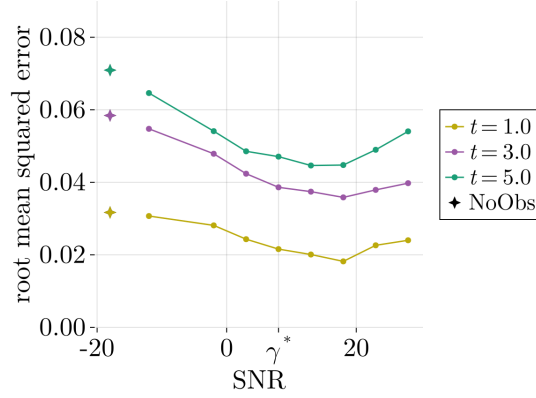


Figure 9: RMSE vs simulated SNR $\gamma = -20 \log_{10} \nu$ with fixed ground-truth SNR $\gamma^* = 8$ dB, $\beta = 96.5 \text{ MPa}^2 \cdot \text{km/MRayl}$, and $\alpha = 1$ at three time steps after the EnKF update. Underestimating the SNR should approach the NoObs case (SNR = $-\infty$) as observations are treated as uninformative. Overestimating the SNR leads to an increase in error because the filter starts to fit the noise.

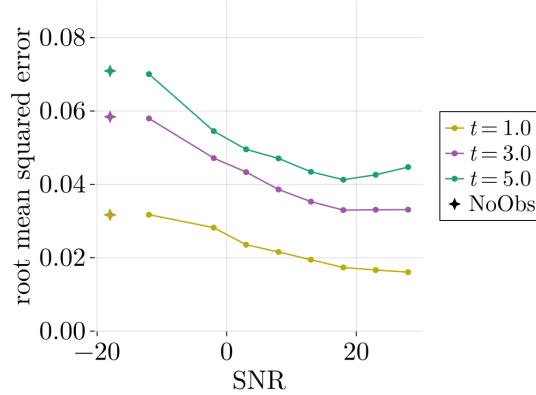


Figure 10: RMSE vs ground-truth SNR $\gamma^* = -20 \log_{10} \nu^*$ with $\nu = \nu^*$ and fixed $\beta = 96.5 \text{ MPa}^2 \cdot \text{km/MRayl}$ and $\alpha = 1$ at three time steps after the EnKF update. Low SNR (large noise) should approach the NoObs case (SNR = $-\infty$) in the two-norm (in expectation). The post-assimilated error increases with SNR at later time steps. That may indicate ν^* does not capture all the sources of noise, meaning there may be noise even when $\nu^* = 0$ due to numerical simulation. To avoid this issue, it may be better to overestimate the noise instead of underestimating it.

6 Conclusion

The existing literature has shown various Kalman filters applied to monitoring CO₂ plume on a relatively small scale or without seismic measurements or without CO₂ dynamics. We apply the EnKF to a high-dimensional CO₂ plume monitored with seismic measurements. We show that it achieves lower error than the non-data-assimilation baselines, which ignore the CO₂ dynamics or ignore the observations. The EnKF is thus a promising tool to use for monitoring CO₂ reservoirs.

In addition to comparing to the two baselines, we also examine the sensitivity of the EnKF to the choice of noise parameters. Lower error is achieved by simulating the observation noise and implicitly obtaining a sample observation noise covariance, compared to approximating the observation noise covariance as a diagonal matrix. Since simulating noise for seismic waveform measurements is inexpensive, we recommend doing this to increase the robustness with respect to the choice of regularization magnitude in the EnKF observation covariance. If the noise is not simulated, we see that the regularization parameter should be chosen based on the largest eigenvalues, not the average standard deviation. Regarding the magnitude of the simulated noise, we find slightly better performance with overestimating the true noise, but this result is specific to the case of relatively low uncertainty in the CO₂ dynamics and may not apply in the general case.

Future work We considered all parameters to be known except for the permeability and the CO₂ saturation and pressure, and we updated only the CO₂ saturation when assimilating observations. Because we do not update the permeability, the error in the EnKF forecast states is very similar to the error from ignoring observations. To achieve accurate predictions of the CO₂ plume, the geological parameters controlling the flow must be updated as well. Therefore, we plan to apply the EnKF to a high-dimensional CO₂ plume with *nonlinear* seismic observations *and* update the permeability and porosity fields along with the CO₂ saturation, following the work of Li *et al.* [69] who updated the permeability and CO₂ saturation with an EnKF variant, Ma *et al.* [26] who updated the permeability and porosity based on the EnKF with approximated seismic images, and Yin *et al.* [51] and Li *et al.* [70] who demonstrated end-to-end inversion for permeability based on time-lapse FWI of CO₂ plumes.

References

- [1] S. Solomon, G. Bureau-Cauchois, N. Ahmed, J. Aarnes, and P. Holtedahl, “CO₂ storage capacity assessment of deep saline aquifers in the mozambique basin,” *Energy Procedia*, vol. 63, pp. 5266–5283, 2014. DOI: 10.1016/j.egypro.2014.11.558.
- [2] A. Raza *et al.*, “Integrity analysis of CO₂ storage sites concerning geochemical-geomechanical interactions in saline aquifers,” *Journal of Natural Gas Science and Engineering*, vol. 36, pp. 224–240, Nov. 2016. DOI: 10.1016/j.jngse.2016.10.016.
- [3] A. Raza, R. Gholami, R. Rezaee, V. Rasouli, and M. Rabiei, “Significant aspects of carbon capture and storage – a review,” *Petroleum*, vol. 5, no. 4, pp. 335–340, Dec. 2019. DOI: 10.1016/j.petlm.2018.12.007.
- [4] C. B. Raleigh, J. H. Healy, and J. D. Bredehoeft, “An experiment in earthquake control at rangely, colorado,” *Science*, vol. 191, no. 4233, pp. 1230–1237, Mar. 26, 1976. DOI: 10.1126/science.191.4233.1230.
- [5] M. He, S. Luis, S. Rita, G. Ana, V. Euripedes, and N. Zhang, “Risk assessment of CO₂ injection processes and storage in carboniferous formations: A review,” *Journal of Rock Mechanics and Geotechnical Engineering*, vol. 3, no. 1, pp. 39–56, Mar. 2011. DOI: 10.3724/SP.J.1235.2011.00039.
- [6] W. J. Stephenson, R. B. Smith, and J. R. Pelton, “A high-resolution seismic reflection and gravity survey of quaternary deformation across the wasatch fault, utah,” *Journal of Geophysical Research: Solid Earth*, vol. 98, pp. 8211–8223, B5 May 10, 1993. DOI: 10.1029/92JB02873.
- [7] G. Gao, A. Abubakar, and T. M. Habashy, “Joint petrophysical inversion of electromagnetic and full-waveform seismic data,” *GEOPHYSICS*, vol. 77, no. 3, WA3–WA18, May 1, 2012. DOI: 10.1190/geo2011-0157.1.
- [8] A. Abubakar, T. M. Habashy, M. Li, and J. Liu, “Inversion algorithms for large-scale geophysical electromagnetic measurements,” *Inverse Problems*, vol. 25, no. 12, p. 123 012, Dec. 1, 2009. DOI: 10.1088/0266-5611/25/12/123012.
- [9] E. S. Um, M. Commer, and G. A. Newman, “A strategy for coupled 3d imaging of large-scale seismic and electromagnetic data sets: Application to subsalt imaging,” *GEOPHYSICS*, vol. 79, no. 3, pp. ID1–ID13, May 1, 2014. DOI: 10.1190/geo2013-0053.1.
- [10] I. Filina *et al.*, “Integration of seismic and gravity data — a case study from the western gulf of mexico,” *Interpretation*, vol. 3, no. 4, SAC99–SAC106, Nov. 1, 2015. DOI: 10.1190/INT-2015-0050.1.
- [11] C. Huang and T. Zhu, “Towards real-time monitoring: Data assimilated time-lapse full waveform inversion for seismic velocity and uncertainty estimation,” *Geophysical Journal International*, vol. 223, no. 2, pp. 811–824, Nov. 1, 2020. DOI: 10.1093/gji/ggaa337.
- [12] D. Grana, M. Liu, and M. Ayani, “Prediction of CO₂ saturation spatial distribution using geostatistical inversion of time-lapse geophysical data,” *IEEE Transactions on Geoscience and Remote Sensing*, vol. 59, no. 5, pp. 3846–3856, May 2021. DOI: 10.1109/TGRS.2020.3018910.
- [13] J. Y. Li, S. Ambikasaran, E. F. Darve, and P. K. Kitanidis, “A kalman filter powered by h2-matrices for quasi-continuous data assimilation problems,” *Water Resources Research*, vol. 50, no. 5, pp. 3734–3749, May 2014. DOI: 10.1002/2013WR014607.
- [14] B. Dupuy, A. Romdhane, P.-L. Nordmann, P. Eliasson, and J. Park, “Bayesian rock-physics inversion: Application to CO₂ storage monitoring,” *GEOPHYSICS*, vol. 86, no. 4, pp. M101–M122, Jul. 1, 2021. DOI: 10.1190/geo2020-0218.1.
- [15] M. Sambridge, “Geophysical inversion with a neighbourhood algorithm—i. searching a parameter space,” *Geophysical Journal International*, vol. 138, no. 2, pp. 479–494, Aug. 1, 1999. DOI: 10.1046/j.1365-246X.1999.00876.x.
- [16] R. N. Bannister, “A review of forecast error covariance statistics in atmospheric variational data assimilation. i: Characteristics and measurements of forecast error covariances,” *Quarterly Journal of the Royal Meteorological Society*, vol. 134, no. 637, pp. 1951–1970, Oct. 2008. DOI: 10.1002/qj.339.
- [17] R. N. Bannister, “A review of forecast error covariance statistics in atmospheric variational data assimilation. II: Modelling the forecast error covariance statistics,” *Quarterly Journal of the Royal Meteorological Society*, vol. 134, no. 637, pp. 1971–1996, Oct. 2008. DOI: 10.1002/qj.340.
- [18] G. Evensen, “The ensemble kalman filter: Theoretical formulation and practical implementation,” *Ocean Dynamics*, vol. 53, no. 4, pp. 343–367, Nov. 1, 2003. DOI: 10.1007/s10236-003-0036-9.

- [19] M. Butala, R. Frazin, Y. Chen, and F. Kamalabadi, “Tomographic imaging of dynamic objects with the ensemble kalman filter,” *IEEE Transactions on Image Processing*, vol. 18, no. 7, pp. 1573–1587, Jul. 2009. DOI: 10.1109/TIP.2009.2017996.
- [20] N. Kumari, R. Kulkarni, M. R. Ahmed, and N. Kumar, “Use of kalman filter and its variants in state estimation: A review,” in *Artificial Intelligence for a Sustainable Industry 4.0*, S. Awasthi, C. M. Travieso-González, G. Sanyal, and D. Kumar Singh, Eds., Springer International Publishing, 2021, pp. 213–230, ISBN: 978-3-030-77070-9. DOI: 10.1007/978-3-030-77070-9_13.
- [21] G. Evensen, “Sampling strategies and square root analysis schemes for the EnKF,” *Ocean Dynamics*, vol. 54, no. 6, pp. 539–560, Dec. 2004. DOI: 10.1007/s10236-004-0099-2.
- [22] K. S. Eikrem, G. Nævdal, and M. Jakobsen, “Iterated extended kalman filter method for time-lapse seismic full-waveform inversion,” *Geophysical Prospecting*, vol. 67, no. 2, pp. 379–394, Jan. 29, 2019. DOI: 10.1111/1365-2478.12730.
- [23] J. Y. Li, A. Kokkinaki, H. Ghorbanidehno, E. F. Darve, and P. K. Kitaniadis, “The compressed state kalman filter for nonlinear state estimation: Application to large-scale reservoir monitoring,” *Water Resources Research*, vol. 51, no. 12, pp. 9942–9963, Dec. 2015. DOI: 10.1002/2015WR017203.
- [24] M. Alfonzo and D. S. Oliver, “Seismic data assimilation with an imperfect model,” *Computational Geosciences*, vol. 24, no. 2, pp. 889–905, Apr. 2020. DOI: 10.1007/s10596-019-09849-0.
- [25] J. D. L. T. Guzman, M. Babaei, J.-Q. Shi, A. Korre, and S. Durucan, “Coupled flow-geomechanical performance assessment of CO₂ storage sites using the ensemble kalman filter,” *Energy Procedia*, vol. 63, pp. 3475–3482, 2014. DOI: 10.1016/j.egypro.2014.11.376.
- [26] W. Ma, B. Jafarpour, and J. Qin, “Dynamic characterization of geologic CO₂ storage aquifers from monitoring data with ensemble kalman filter,” *International Journal of Greenhouse Gas Control*, vol. 81, pp. 199–215, Feb. 2019. DOI: 10.1016/j.ijggc.2018.10.009.
- [27] M. Tang, X. Ju, and L. J. Durlofsky, “Deep-learning-based coupled flow-geomechanics surrogate model for CO₂ sequestration,” *International Journal of Greenhouse Gas Control*, vol. 118, p. 103692, Jul. 2022. DOI: 10.1016/j.ijggc.2022.103692.
- [28] M. Tang, Y. Liu, and L. J. Durlofsky, “A deep-learning-based surrogate model for data assimilation in dynamic subsurface flow problems,” *Journal of Computational Physics*, vol. 413, p. 109456, Jul. 2020. DOI: 10.1016/j.jcp.2020.109456.
- [29] G. S. Seabra, N. T. Mücke, V. L. S. Silva, D. Voskov, and F. C. Vossepoel, “AI enhanced data assimilation and uncertainty quantification applied to geological carbon storage,” *International Journal of Greenhouse Gas Control*, vol. 136, p. 104190, Jul. 2024. DOI: 10.1016/j.ijggc.2024.104190.
- [30] H. Tang *et al.*, “A deep learning-accelerated data assimilation and forecasting workflow for commercial-scale geologic carbon storage,” *International Journal of Greenhouse Gas Control*, vol. 112, p. 103488, Dec. 2021. DOI: 10.1016/j.ijggc.2021.103488.
- [31] H. Tang *et al.*, “Deep learning-accelerated 3d carbon storage reservoir pressure forecasting based on data assimilation using surface displacement from InSAR,” *International Journal of Greenhouse Gas Control*, vol. 120, p. 103765, Oct. 2022. DOI: 10.1016/j.ijggc.2022.103765.
- [32] Z. Yin, A. Siahkoohi, M. Louboutin, and F. J. Herrmann, “Learned coupled inversion for carbon sequestration monitoring and forecasting with fourier neural operators,” in *Second International Meeting for Applied Geoscience & Energy*, ser. SEG Technical Program Expanded Abstracts, Society of Exploration Geophysicists and American Association of Petroleum Geologists, Aug. 8, 2022, pp. 467–472. DOI: 10.1190/image2022-3722848.1.
- [33] M. Liu, D. Vashisth, D. Grana, and T. Mukerji, “Joint inversion of geophysical data for geologic carbon sequestration monitoring: A differentiable physics-informed neural network model,” *Journal of Geophysical Research: Solid Earth*, vol. 128, no. 3, e2022JB025372, Mar. 2023. DOI: 10.1029/2022JB025372.
- [34] T. Sakai, M. Nagao, C. H. Chan, A. Datta-Gupta, and C. Yao, “CO₂ plume imaging with accelerated deep learning-based data assimilation using distributed pressure and temperature measurements at the illinois basin-decatur carbon sequestration project,” in *Proceedings of the 2024 Carbon Capture, Utilization, and Storage Conference*, American Association of Petroleum Geologists, 2024, ISBN: 978-1-73619-224-5. DOI: 10.15530/ccus-2024-4014874.
- [35] A. P. Gahlot, H. T. Erdinc, R. Orozco, Z. Yin, and F. J. Herrmann, *Inference of CO₂ flow patterns – a feasibility study*, Version Number: 2, 2023. DOI: 10.48550/ARXIV.2311.00290.
- [36] A. P. Gahlot, H. Li, Z. Yin, R. Orozco, and F. J. Herrmann, *A digital twin for geological carbon storage with controlled injectivity*, Version Number: 1, 2024. DOI: 10.48550/ARXIV.2403.19819.
- [37] R. E. Kalman, “A new approach to linear filtering and prediction problems,” *Journal of Basic Engineering*, vol. 82, no. 1, pp. 35–45, Mar. 1, 1960. DOI: 10.1115/1.3662552.
- [38] G. L. Smith, S. F. Schmidt, and L. A. McGee, “Application of statistical filter theory to the optimal estimation of position and velocity on board a circumlunar vehicle,” National Aeronautics and Space Administration, Technical Report 19620006857, 1962.
- [39] J. Valappil and C. Georgakis, “Systematic estimation of state noise statistics for extended kalman filters,” *AIChE Journal*, vol. 46, no. 2, pp. 292–308, Feb. 2000. DOI: 10.1002/aic.690460209.
- [40] G. Evensen, “Sequential data assimilation with a nonlinear quasi-geostrophic model using monte carlo methods to forecast error statistics,” *Journal of Geophysical Research: Oceans*, vol. 99, pp. 10143–10162, C5 May 15, 1994. DOI: 10.1029/94JC00572.

- [41] G. Burgers, P. Jan Van Leeuwen, and G. Evensen, “Analysis scheme in the ensemble kalman filter,” *Monthly Weather Review*, vol. 126, no. 6, pp. 1719–1724, Jun. 1998. DOI: 10.1175/1520-0493(1998)126<1719:ASITEK>2.0.CO;2.
- [42] J. L. Anderson and S. L. Anderson, “A monte carlo implementation of the nonlinear filtering problem to produce ensemble assimilations and forecasts,” *Monthly Weather Review*, vol. 127, no. 12, pp. 2741–2758, Dec. 1999. DOI: 10.1175/1520-0493(1999)127<2741:AMCIOT>2.0.CO;2.
- [43] T. M. Hamill and C. Snyder, “A hybrid ensemble kalman filter–3d variational analysis scheme,” *Monthly Weather Review*, vol. 128, no. 8, pp. 2905–2919, Aug. 2000. DOI: 10.1175/1520-0493(2000)128<2905:AHEKFB>2.0.CO;2.
- [44] J. S. Whitaker and T. M. Hamill, “Ensemble data assimilation without perturbed observations,” *Monthly Weather Review*, vol. 130, no. 7, pp. 1913–1924, Jul. 2002. DOI: 10.1175/1520-0493(2002)130<1913:EDAWPO>2.0.CO;2.
- [45] J. S. Whitaker, G. P. Compo, X. Wei, and T. M. Hamill, “Reanalysis without radiosondes using ensemble data assimilation,” *Monthly Weather Review*, vol. 132, no. 5, pp. 1190–1200, May 2004. DOI: 10.1175/1520-0493(2004)132<1190:RWRUED>2.0.CO;2.
- [46] A. Y. Beliaev and S. M. Hassanizadeh, “A theoretical model of hysteresis and dynamic effects in the capillary relation for two-phase flow in porous media,” *Transport in Porous Media*, vol. 43, no. 3, pp. 487–510, 2001. DOI: 10.1023/A:1010736108256.
- [47] C. MacBeth, “A classification for the pressure-sensitivity properties of a sandstone rock frame,” *GEOPHYSICS*, vol. 69, no. 2, pp. 497–510, Mar. 2004. DOI: 10.1190/1.1707070.
- [48] G. Côte, H. Amini, and C. MacBeth, “Bayesian inversion of 4d seismic data to pressure and saturation changes: Application to a west of shetlands field,” *Geophysical Prospecting*, vol. 71, no. 2, pp. 292–321, Feb. 2023. DOI: 10.1111/1365-2478.13304.
- [49] P. Avseth, T. Mukerji, and G. Mavko, *Quantitative seismic interpretation: Applying rock physics tools to reduce interpretation risk*. Cambridge university press, 2010.
- [50] F. Gassmann, “Über die elastizität poroser medien,” *Vierteljahrsschrift der Naturforschenden Gesellschaft in Zurich*, vol. 96, pp. 1–23, 1951.
- [51] Z. Yin, M. Louboutin, O. Møyner, and F. J. Herrmann, *Time-lapse full-waveform permeability inversion: A feasibility study*, Version Number: 1, 2024. DOI: 10.48550/ARXIV.2403.04083.
- [52] O. Møyner, B. M. Pacheco, A. Riedemann, G. Bruer, T. Holy, and Z. Yin, *Sintefmath/JutulDarcy.jl: V0.2.11*, version v0.2.11, Nov. 17, 2023. DOI: 10.5281/ZENODO.10150938.
- [53] O. Møyner, M. Johnsrud, H. M. Nilsen, X. Raynaud, K. O. Lye, and Z. Yin, *Sintefmath/jutul.jl: V0.2.16*, version v0.2.16, Nov. 17, 2023. DOI: 10.5281/ZENODO.10150601.
- [54] F. J. Herrmann, C. R. Brown, Y. A. Erlangga, and P. P. Moghaddam, “Curvelet-based migration preconditioning and scaling,” *GEOPHYSICS*, vol. 74, no. 4, A41–A46, Jul. 2009. DOI: 10.1190/1.3124753.
- [55] P. A. Witte *et al.*, “A large-scale framework for symbolic implementations of seismic inversion algorithms in julia,” *GEOPHYSICS*, vol. 84, no. 3, F57–F71, May 1, 2019. DOI: 10.1190/geo2018-0174.1.
- [56] M. Louboutin *et al.*, *Slinggroup/JUDI.jl: V3.3.10*, version v3.3.10, Jan. 23, 2024. DOI: 10.5281/ZENODO.10556864.
- [57] M. Louboutin *et al.*, “Devito (v3.1.0): An embedded domain-specific language for finite differences and geophysical exploration,” *Geoscientific Model Development*, vol. 12, no. 3, pp. 1165–1187, Mar. 27, 2019. DOI: 10.5194/gmd-12-1165-2019.
- [58] F. Luporini *et al.*, “Architecture and performance of devito, a system for automated stencil computation,” *ACM Transactions on Mathematical Software*, vol. 46, no. 1, pp. 1–28, Mar. 31, 2020. DOI: 10.1145/3374916.
- [59] L. R. Lines, R. Slawinski, and R. P. Bording, “A recipe for stability of finite-difference wave-equation computations,” *GEOPHYSICS*, vol. 64, no. 3, pp. 967–969, May 1999. DOI: 10.1190/1.1444605.
- [60] M. Schmidt, E. Berg, M. Friedlander, and K. Murphy, “Optimizing costly functions with simple constraints: A limited-memory projected quasi-newton algorithm,” in *Proceedings of the Twelfth International Conference on Artificial Intelligence and Statistics*, D. van Dyk and M. Welling, Eds., ser. Proceedings of Machine Learning Research, vol. 5, PMLR, Apr. 16, 2009, pp. 456–463.
- [61] M. Louboutin, Z. Yin, and F. Herrmann, *Slinggroup/SlimOptim.jl: V0.2.5*, version v0.2.5, Mar. 19, 2024. DOI: 10.5281/ZENODO.10839737.
- [62] L. I. Rudin, S. Osher, and E. Fatemi, “Nonlinear total variation based noise removal algorithms,” *Physica D: Nonlinear Phenomena*, vol. 60, no. 1, pp. 259–268, Nov. 1992. DOI: 10.1016/0167-2789(92)90242-F.
- [63] A. N. Tikhonov and V. Y. Arsenin, *Solutions of ill-posed problems*. V. H. Winston & Sons, 1977, xiii+258.
- [64] K. P. Bube and R. T. Langan, “Hybrid ℓ_1/ℓ_2 minimization with applications to tomography,” *GEOPHYSICS*, vol. 62, no. 4, pp. 1183–1195, Jul. 1997. DOI: 10.1190/1.1444219.
- [65] R. Modrak and J. Tromp, “Seismic waveform inversion best practices: Regional, global and exploration test cases,” *Geophysical Journal International*, vol. 206, no. 3, pp. 1864–1889, Sep. 1, 2016. DOI: 10.1093/gji/ggw202.
- [66] C. E. Jones, J. A. Edgar, J. I. Selva, and H. Crook, “Building complex synthetic models to evaluate acquisition geometries and velocity inversion technologies,” presented at the 74th EAGE Conference and Exhibition incorporating EUROPEC 2012, Jun. 4, 2012. DOI: 10.3997/2214-4609.20148575.
- [67] M. D. Bloice, C. Stocker, and A. Holzinger, *Augmentor: An image augmentation library for machine learning*, Aug. 11, 2017. arXiv: 1708.04680 [cs, stat].

- [68] Z. Wang, A. Bovik, H. Sheikh, and E. Simoncelli, "Image quality assessment: From error visibility to structural similarity," *IEEE Transactions on Image Processing*, vol. 13, no. 4, pp. 600–612, Apr. 2004. DOI: 10.1109/TIP.2003.819861.
- [69] J. Y. Li, A. Kokkinaki, E. F. Darve, and P. K. Kitanidis, "Smoothing-based compressed state Kalman filter for joint state-parameter estimation: Applications in reservoir characterization and CO₂ storage monitoring," *Water Resources Research*, vol. 53, no. 8, pp. 7190–7207, Aug. 2017. DOI: 10.1002/2016WR020168.
- [70] D. Li, K. Xu, J. M. Harris, and E. Darve, "Coupled time-lapse full-waveform inversion for subsurface flow problems using intrusive automatic differentiation," *Water Resources Research*, vol. 56, no. 8, Aug. 2020. DOI: 10.1029/2019WR027032.